RESEARCH ARTICLE

Key Points:
- The simulated AMOC has significant discrepancy in ECHAM6-FESOM/MPIOM with different resolutions
- Atmospheric hydrological cycle and sea ice transport are sensitive processes for AMOC
- Most CMIP5 models show a stronger-than-present AMOC in the mid-Holocene

Supporting Information:
- Supporting Information S1

Correspondence to:
X. Shi,
xshi@awi.de

Simulated response of the mid-Holocene Atlantic meridional overturning circulation in ECHAM6-FESOM/MPIOM

Xiaoxu Shi[1] and Gerrit Lohmann[1,2]

[1]Alfred Wegener Institute, Helmholtz Center for Polar and Marine Research, Bremerhaven, Germany, [2]University of Bremen, Bremen, Germany

Abstract Changes of the Atlantic meridional overturning circulation (AMOC) in the mid-Holocene compared to the preindustrial state are explored in different coupled climate models. Using time-slice integrations by a newly developed global finite-element model ECHAM6-FESOM with unstructured mesh and high resolution, our simulations show an enhanced mid-Holocene AMOC, accompanied by an increase in the ocean salinity over regions of deep water formation. We identify two different processes affecting the AMOC: (1) a more positive phase of North Atlantic Oscillation (NAO) increased water density over the Labrador Sea through anomalous net evaporation and surface heat loss; (2) a decreased import of sea ice from the Arctic causes a freshwater reduction in the northern North Atlantic Ocean. Using the coupled model ECHAM6-MPIOM in T63GR15 and T31GR30 grids, we find that the simulated AMOC has significant discrepancy with different model resolutions. In detail, stronger-than-present mid-Holocene AMOC is revealed by simulations with the T63GR15 grid, which resembles the result of ECHAM6-FESOM, while a decline of the mid-Holocene AMOC is simulated by the low resolution model with the T31GR30 grid. Such discrepancy can be attributed to different changes in Labrador Sea density which is mainly affected by (1) NAO-induced net precipitation and deep water convection, (2) freshwater transport from the Arctic Ocean, and (3) the strength of AMOC itself. Finally, we analyzed available coupled climate models showing a diversity of responses of AMOC to mid-Holocene forcings, most of which reveal positive AMOC changes related to northern high latitudes salinification.

1. Introduction

There are multiple lines of evidence that variations in the North Atlantic meridional overturning circulation (AMOC) is a major source of decadal and multidecadal variability in the climate system. Prominently, this is manifested in the sea surface temperature and salinity over North Atlantic. An abundance of studies [e.g., *Schlesinger and Ramankutty*, 1994; *Rühlemann et al.*, 2004; *Knight et al.*, 2005; *Dima and Lohmann*, 2007; *Parker et al.*, 2007; *Zhang*, 2007, 2008; *Chylek et al.*, 2009] provided rigorous evidence of the widely hypothesized link between the AMOC and the Northern Hemisphere mean surface temperature, as well as the Arctic surface air temperature (SAT). Using observational data, *Polyakov et al.* [2005] demonstrated that temperature and salinity from the 0–300 to 1000–3000 m layers vary in opposition: prolonged periods of cooling and freshening (warming and salinification) in one layer are generally associated with opposite tendencies in the other layer, which may be associated with a change in the strength of AMOC. *Parker et al.* [2007] analyzed modeling results and represented a mechanism for feedback between weak (strong) AMOC and cooler (warmer) North Atlantic. Another source of multidecadal oscillation is attributed to stochastic forcing from the midlatitude atmospheric circulation, with thermal coupling playing a role in the tropics [*Clement et al.*, 2015].

The mid-Holocene (6k) is one of the key times in the past to test models [e.g., *Crucifix et al.*, 2005; *Braconnot et al.*, 2007]. The most prominent difference between 6k and present arises from the orbital configuration, which leads to an increase in boreal summer insolation in the Northern Hemisphere (NH) and a decrease in the tropical and subtropical Southern Hemisphere in boreal winter [*Lohmann et al.*, 2013]. Reproducing AMOC of 6k is not only scientifically interesting in itself, but also of crucial importance to increase our understanding of the climate responses to external forcings involving the orbital parameters and greenhouse gases concentrations. So far, many efforts have been made to simulate the 6k AMOC. For example,

Ganopolski et al. [1998] and *Otto-Bliesner et al.* [2006] produced weaker-than-present AMOC for the mid-Holocene with the climate models CLIMBER and CCSM3 respectively. *Wei and Lohmann* [2012] simulated a difference of −2 Sv between the AMOC of mid-Holocene and preindustrial using the coupled model ECHAM5-MPIOM with a coarse-resolution grid. The same result is also found by *Fischer and Jungclaus* [2010] who performed similar simulations using ECHAM5-MPIOM with a different vegetation code and without the implementation of 6k greenhouse gases. *Zheng and Yu* [2013] simulated the climate condition of 6k with different versions of the coupled model FGOALS, and found a weakened (enhanced) AMOC during 6k with old (new) version of the model. Furthermore, different results are shown by *Renssen et al.* [2005] who demonstrated a long-term reduction from the Holocene to present in maximum meridional overturning with the model ECBilt-CLIOVECODE.

In the present paper, we are specifically interested in the sensitivity of AMOC to different model components and resolutions. The importance of model resolution has been described in several studies [e.g., *Boville*, 1991; *Buizza et al.*, 1998]. So far the publications of the mid-Holocene AMOC were mostly based on coarse or regular resolution models, e.g., CLIMBER (10° × 51° for ocean component), ECHO-G (3.8° × 3.8°), COSMOS (3° × 3°), ECBilt-CLIOVECODE (3° × 3°), and FGOALS (1° × 1°). Therefore, in the convection areas the water masses might not be well represented in these models. Utilization of a newly developed global climate model ECHAM6-FESOM with unstructured mesh and high resolution [*Sidorenko et al.*, 2014] allows a more comprehensive simulation for examining the mid-Holocene AMOC, and for exploring the mechanism behind the AMOC change. Furthermore, we investigate the response of AMOC to model resolutions by analyzing results of the climate model ECHAM6-MPIOM with two different resolutions.

This article is organized as follows. We briefly introduce the models used in this study and our experimental design in section 2. In the third chapter, we present the simulation results and we discuss and conclude in sections 4 and 5, respectively.

2. Model Description and Experimental Design

2.1. ECHAM6-FESOM

ECHAM6-FESOM is a newly developed global coupled climate model which has been established at the Alfred Wegener Institute (AWI). The ocean-sea ice component is the Finite Element Sea Ice-Ocean Model (FESOM) [*Danilov et al.*, 2004; *Timmermann et al.*, 2009; *Sidorenko et al.*, 2011; *Wang et al.*, 2013; *Sidorenko et al.*, 2014] which is discretized on a triangular grid with a continuous conforming representation of model variables, whereas the atmospheric module is represented by the general circulation model ECHAM6 [*Stevens et al.*, 2013], mainly developed by the Max Planck Institute for Meteorology (MPI-M).

ECHAM6 is the sixth generation of the atmospheric general circulation model ECHAM, focusing on the coupling between diabatic processes, which is often associated with small-scale fluid dynamics, and large-scale circulations. The model is branched from an early release of the European Center (EC) for Medium Range Weather Forecasts (ECMWF) model [*Roeckner et al.*, 1989]. Like most models, the dynamics of ECHAM6 is based on the hydrostatic primitive equations (HPEs) with traditional approximation. Gaussian grid is used in the model to calculate nonlinear equation terms and some physical representation. The boundary layer and turbulence parameterization is based on the eddy diffusivity/viscosity approach. Momentum transport arising from boundary effects is parameterized using the subgrid orography scheme as described by *Lott* [1999]. Subgrid-scale cloudiness is represented using the assumed humidity distribution function scheme developed by *Sundqvist et al.* [1989]. Radiative transfer in ECHAM6 is represented using the rapid radiation transfer [*Iacono et al.*, 2008]. ECHAM6 also includes a Land-Surface Model (JSBACH) which includes dynamic vegetation with 12 plant functional types and two types of bare surface [*Loveland et al.*, 2000; *Raddatz et al.*, 2007]. ECHAM6-FESOM is configured on T63L47 grid for the atmosphere, which is 1.9° for horizontal resolution and 47 levels in vertical direction.

FESOM is a hydrostatic ocean circulation model based on the finite-element approach and designed to work on unstructured meshes, therefore is different in many important ways from models formulated on regular meshes. The mesh nodes are vertically aligned to avoid difficulties in resolving the hydrostatic balance. The model uses variable resolution from about 200 km in the open ocean to 20 km along coastlines as shown in Figure 1a, with 40,309 surface nodes. A no-slip boundary condition along the coast is implemented in the model. There are 46 vertical levels. Surface stress and buoyancy fluxes are derived from the
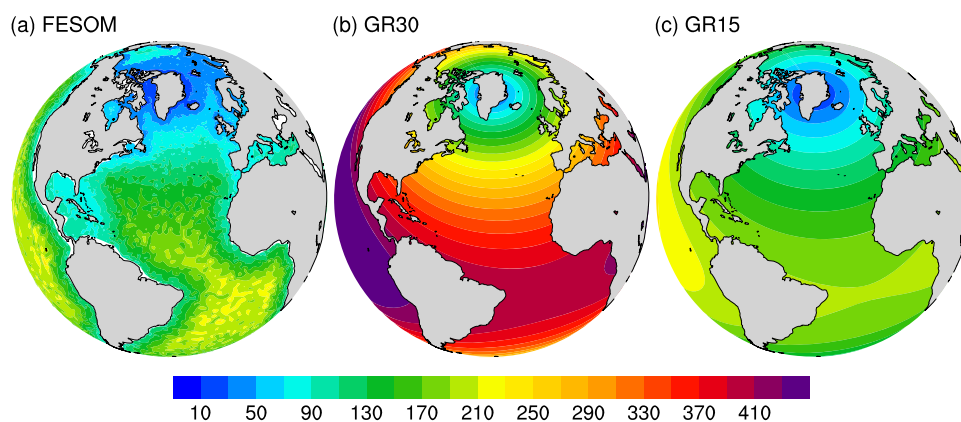
(a) FESOM   (b) GR30   (c) GR15

10 50 90 130 170 210 250 290 330 370 410

Figure 1. Resolution applied in our experiments. Units are km.

ice-ocean coupling. The FESOM sea ice component is a dynamic-thermodynamic sea ice model with the *Parkinson and Washington* [1979] thermodynamics. The model consists of subgrid-scale processes based on *Redi* [1982], a so-called zero-layer approach of [*Semtner*, 1976] and a submodel of ice dynamics according to an elastic-viscous-plastic rheology [*Hunke and Dukowicz*, 1997]. The model also includes a prognostic snow layer [*Owens and Lemke*, 1990]. The paramerization of snow-ice conversion is based on *Leppäranta* [1983]. FESOM model has been validated in *Timmermann et al.* [2009] and *Scholz et al.* [2013].

2.2. ECHAM6-MPIOM

Besides ECHAM6-FESOM, we also conduct experiments using the coupled model ECHAM6-MPIOM [*Stevens et al.*, 2013; *Jungclaus et al.*, 2013]. The ocean general circulation model MPIOM is based on the primitive equations with representation of dynamic and thermodynamic processes. MPIOM uses a curvilinear orthogonal grid which allows for a variety of configurations. ECHAM6-MPIOM employs the overflow method given by *Whitehead* [1998]. A detailed description is given by *Marsland et al.* [2003]. The coupled model has been developed for several resolutions, for example, the atmosphere component can be configured on T31, T63, T127, and T255 grids, associated with Gaussian grids of approximately 3°, 1.9°, 0.95°, and 0.47° resolution, respectively [*Stevens et al.*, 2013]. The ocean model MPIOM has several grid options such as GR30 (3°), GR15 (1.5°), TP04 (0.4°), and TP6M (0.1°) [*Marsland et al.*, 2003; *Storch et al.*, 2012]. In addition, ECHAM6-MPIOM has a subsystem model for land and vegetation JSBACH [*Reick et al.*, 2013; *Schneck et al.*, 2013]. In this study, ECHAM6-MPIOM applies 31 and 40 vertical levels for the atmosphere and ocean, respectively.

2.3. Experimental *Design*

In the following, we describe the experimental setup of our simulations. A summary of the experiment characteristics is also provided in Table 1. For each model configuration, we have two time-slice experiments, a preindustrial control experiment and a mid-Holocene one. The atmospheric model is initialized by the mean climatology from an Atmospheric Model Intercomparison Project (AMIP)-style experiment, which is performed using observed monthly sea surface temperatures and sea ice cover for the period 1978–1999 [*Roeckner et al.*, 2004]. The ice-ocean model is initialized by the data from the World Ocean Atlas (WOA). The boundary conditions, orbital parameters and Greenhouse gases (GHGs) are prescribed according to the Paleoclimate Modeling Intercomparison Project (PMIP) [*Crucifix et al.*, 2005]. For each time period and experiment, the models are run long enough for the trends over the final years to be small. To define the representative climatology, we employed the quasi-equilibrium criteria of the PMIP protocol [*Braconnot et al.*, 2007] to assess the stability of the simulated ocean states, which is, quasi-equilibrium state can be achieved with global sea surface temperature trend being less than 0.05°C/century. ECHAM6-FESOM experiments are integrated for 700 years in T63 resolution (1.9° × 1.9°) for the atmosphere component and varying resolution as shown in Figure 1a for the ice-ocean component. The model has run into quasi-equilibrium with trends in sea surface temperature that do not exceed 0.02°C/century for the model years 501–700. Therefore, the average of the last 200 model years is considered to represent the climatology in both simulations. For comparison with the result of ECHAM6-FESOM, we conduct another two experiment EM31-CTR (a preindustrial control setup) and EM31-6k (a mid-Holocene setup) using the ECHAM6-MPIOM model with low-resolution grid (T31GR30). The simulations are integrated for 700

Table 1. List of Experiments and Boundary Conditions

Experiment	EF-CTR	EF-6k	EM31-CTR	EM31-6k	EM63-CTR	EM63-6k
Model	ECHAM6-FESOM	ECHAM6-FESOM	ECHAM6-MPIOM	ECHAM6-MPIOM	ECHAM6-MPIOM	ECHAM6-MPIOM
Atmosphere grid	T63	T63	T31	T31	T63	T63
Ocean grid	Figure 1	Figure 1	GR30	GR30	GR15	GR15
CO2 (ppm)	280	280	280	280	280	280
CH4 (ppb)	760	650	760	650	760	650
N2O (ppb)	270	270	270	270	270	270
Eccentricity	0.016724	0.018682	0.016724	0.018682	0.016724	0.018682
Obliquity	23.446	24.105	23.446	24.105	23.446	24.105
Precession	282.04	180.87	282.04	180.87	282.04	180.87
Integration Time (a)	700(200)	700(200)	700(200)	700(200)	3000(200)	2000(100)

model years with final trends in sea surface temperature being less than 0.01°C/century. Furthermore, in order to highlight the importance of model resolution, we also analyze in detail the ECHAM6-MPIOM output in T63GR15 grid from the Coupled Model Intercomparison Project Phase 5 (CMIP5) data set. It has been integrated for 3000 and 2000 years, with final trends in sea surface temperature being 0.013°C/century and −0.0001°C/century for 0k and 6k experiment, respectively. For preindustrial, we take the final 200 years data for analysis, whereas for 6k only 100 model years outputs are available in CMIP5. The resolution distributions for ocean components are shown in Figures 1b and 1c. More detailed information about the experimental configuration is presented in Table 1.

2.4. Other Model Data Used

We process preindustrial and mid-Holocene climatology data from nine other climate models in the CMIP5 archive [*Taylor et al.*, 2012] to have a further view of the AMOC change. Detailed information of the nine models we used here is summarized in Table 2.

3. Results

In this section, we concentrate on the behavior of the high-resolution model ECHAM6-FESOM (experiments EF-CTR and EF-6k). For comparison, we also show results of ECHAM6-MPIOM in low-resolution grid T31GR30 (experiments EM31-CTR and EM31-6k) as well as ECHAM6-MPIOM with T63GR15, which is referred to as EM63-CTR for preindustrial and EM63-6k for mid-Holocene (part of CMIP5). The results of other CMIP5 models are shown in section 3.5.

The seasonal and annual mean climatology is calculated by averaging the climate parameters over the integration periods given in Table 1.

3.1. Atlantic Meridional Overturning Circulation

In EF-CTR, the Atlantic meridional overturning circulation (AMOC) stream function, defined as the zonally integrated stream function over the Atlantic basin, has the maximum of 13.4 Sv (1 Sv = 10^6 m^3/s) at 1000 m depth of 35°N (Figure 2a), consistent with the estimates of global circulation from the hydrographic data (15 ± 3 Sv) [*Ganachaud and Wunsch*, 2000]. This value increases by 1–2 Sv in the EF-6k (Figure 2b), and the position of the maximum AMOC shifts northward.

Table 2. List of CMIP5 Model Data

Name	Reference	Resolution (Atmosphere, Ocean)
BCC-CSM1-1	*Wu et al.* [2008, 2010]	(1° × 1°, 1.5° × 1.5°)
CCSM4	*Gent et al.* [2011]	(1° × 1°, 0.5° × 1.1°)
CNRM-CM5	*Voldoire et al.* [2013]	(1.4° × 1.4°, 1° × 1°)
CSIRO-Mk3-6-0	*Collier et al.* [2011]	(1.9° × 1.9°, 1° × 2°)
FGOALS-g2	*Li et al.* [2013]	(2.8° × 2.8°, 1° × 1°)
FGOALS-s2	*Bao et al.* [2013]	(1.65° × 2.8°, 1° × 1°)
GISS-E2-R	*Schmidt et al.* [2014]	(2° × 2.5°, 1° × 1°)
MIROC-ESM	*Watanabe et al.* [2011]	(2.8° × 2.8°, 1° × 1.4°)
MRI-CGCM3	*Yukimoto et al.* [2012]	(1.1° × 1.1°, 1° × 0.5°)

Regarding the behavior of ECHAM6-MPIOM, the maximum AMOC stream function happens at 1000 m depth between 30°N and 35°N, with the magnitude of 14 and 20 Sv for coarse and higher resolution model, respectively. Different AMOC tendencies are observed as depicted in Figures 2b and 2c: with coarse-resolution (T31GR30), EM31-6k reproduces a decline in AMOC with a magnitude of about −2 Sv compared to EM31-CTR, similar to the
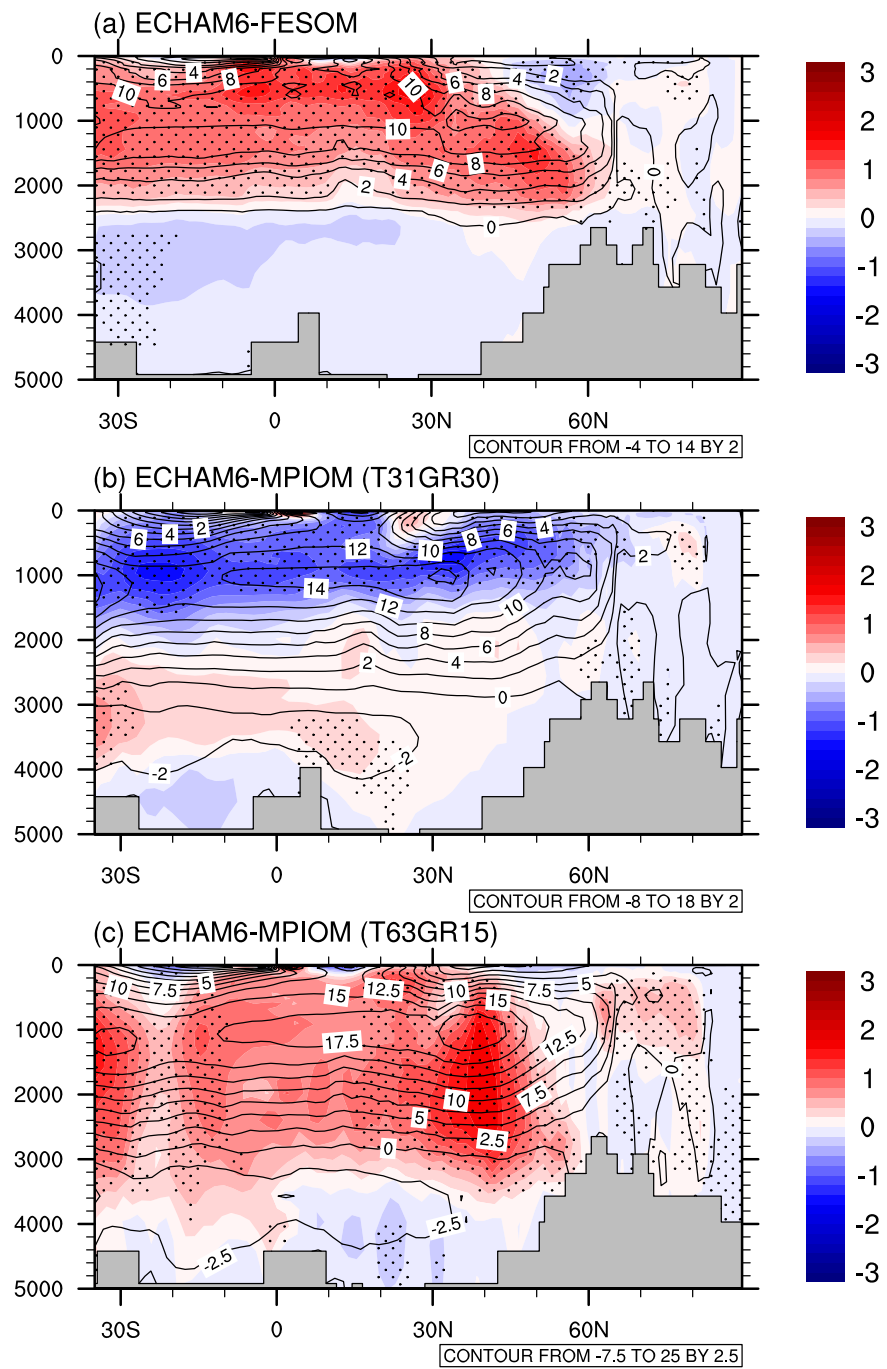
Figure 2. Simulated annual mean Atlantic meridional overturning circulation (contour lines) and its anomalies in mid-Holocene compared to preindustrial (shading colors) based on (a) ECHAM6-FESOM, (b) ECHAM6-MPIOM with T31GR30 grid, and (c) ECHAM6-MPIOM with T63GR15 grid. Regions with >95% significance level (based on Student's t-test) are hatched by black dots, auto-correlation has been taken into account. Units are Sv.

T31GR30 setup by ECHAM5-MPIOM [*Fischer and Jungclaus*, 2010; *Wei and Lohmann*, 2012]. In contrast, the T63GR15 version of ECHAM6-MPIOM shows an increase in AMOC (2 Sv), which is similar to the result of ECHAM6-FESOM.

In summary, we detect big discrepancies of simulated AMOC anomalies between models with coarse (T31GR30) and higher (T63GR15) resolutions. Therefore, model resolution is an important factor which is explored in the following.

3.2. Properties of the North Atlantic Ocean

The North Atlantic Ocean is a critical region for the AMOC since its variability can change sea-water properties in particular the density in the sinking region of the North Atlantic deep water formation sites and thus affects the strength of the AMOC.

The simulated North Atlantic temperature, salinity, and density and their respective difference distributions in mid-Holocene compared to preindustrial are given in Figure 3. The distribution of sea surface temperature (SST) anomalies in ECHAM6-FESOM is characterized by a warming over the North Atlantic Ocean, Baffin Bay and Nordic Sea (Figure 3a). It is attributed mainly to increased insolation in boreal summer, which is induced by a larger tilt of the orbital plane. The most intriguing change happens over the Gulf Stream, where the largest SST gradient occurs. The sea surface salinity (SSS) anomalies in ECHAM6-FESOM (Figure 3d) presents a freshening Arctic Ocean (up to −0.5 psu), which is related to a smaller sea ice production. Compared to preindustrial conditions, more saline seawater is simulated in the GIN (Greenland, Iceland, Norwegian) Sea, and the North Atlantic subpolar region (0.5 psu). More pronounced salinification is observed over the Gulf Stream (more than 0.5 psu), which is connected to the strengthening of surface northward current and the northward replacement of the Gulf Stream in mid-Holocene. The corresponding density change in ECHAM6-FESOM resembles the SSS pattern, with negative anomalies over the Arctic Ocean and positive anomalies over the North Atlantic Ocean and Nordic Sea (Figure 3g).

ECHAM6-MPIOM in both grids reveal a general warming in 6k over the Baffin Bay and Nordic Sea (Figures 3b and 3c), compared to the preindustrial conditions. A significant cooling is simulated by EM31-6k over
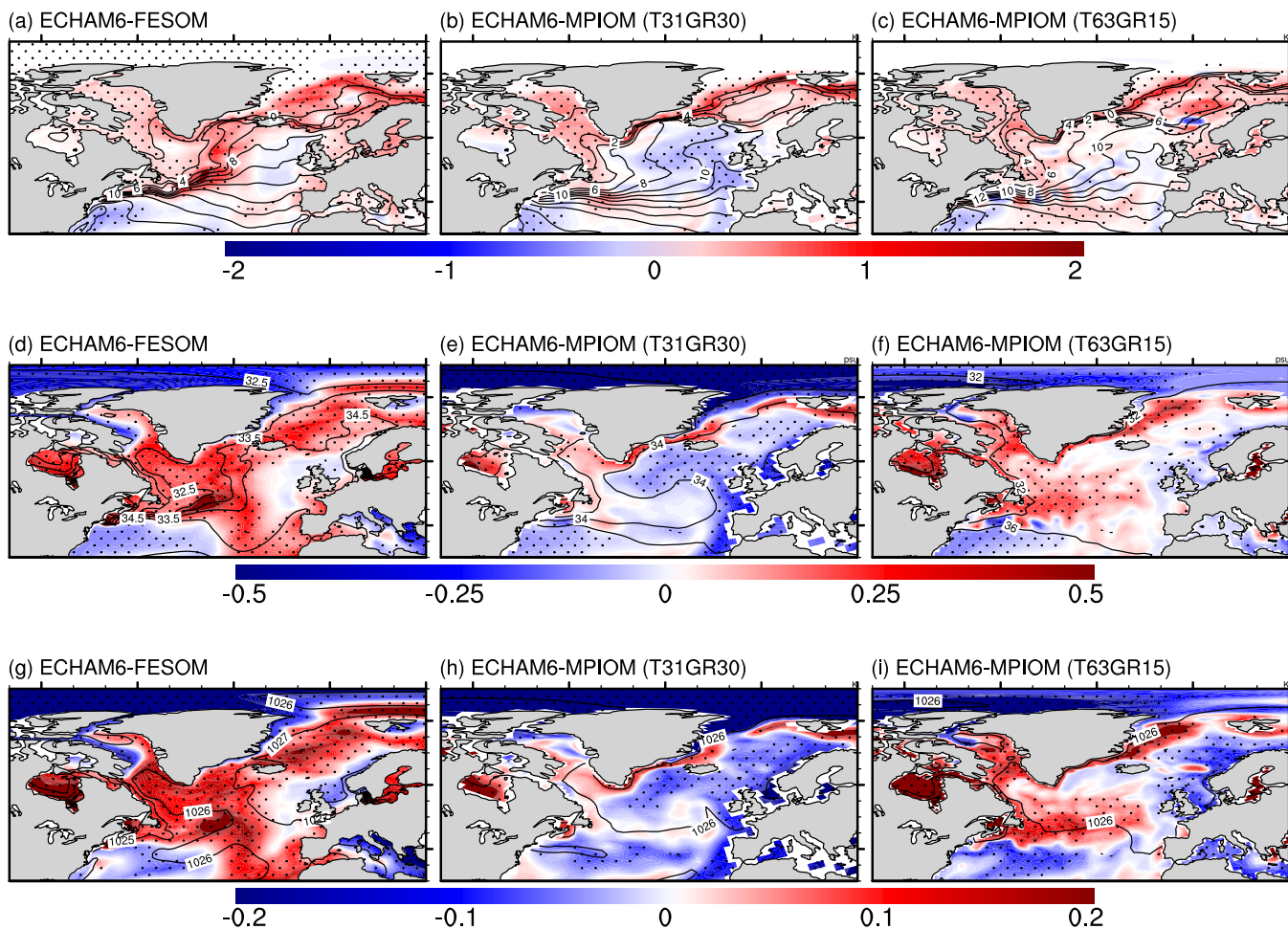

Figure 3. Simulated annual mean anomalies for (a–c) sea surface temperature, (d–f) sea surface salinity, and (g–i) sea surface density over the North Atlantic Ocean. Units are °C, psu, and kg/m³, respectively. Coutour lines in each panel represent the corresponding absolute values in control experiment. Regions with >95% significance level (based on Student's *t*-test) are hatched by black dots.
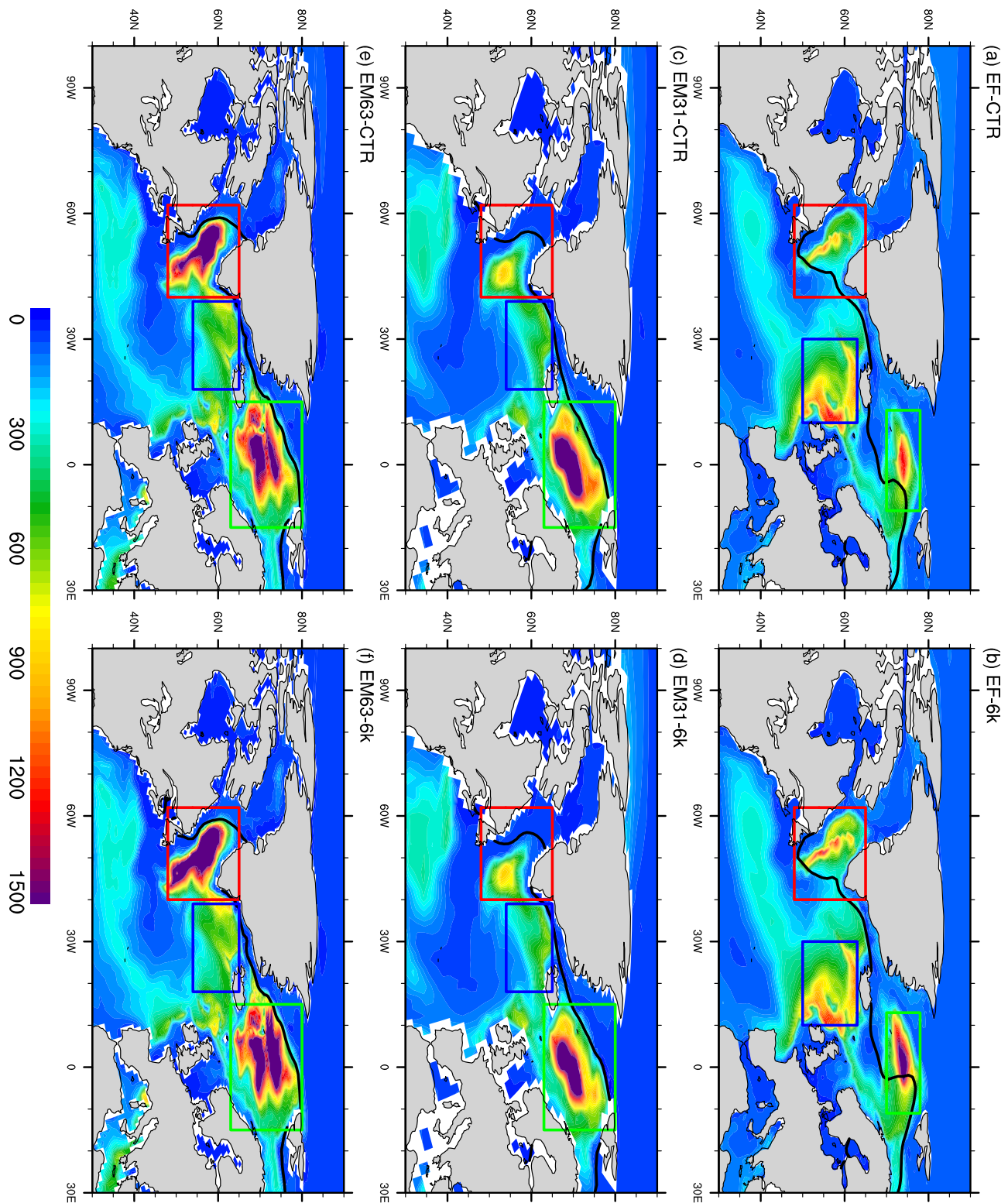
Figure 4. MLD simulated in all experiments. Units are m. Solid contour indicates the ice extent, defined by 15% sea ice concentration.

the North Atlantic, particularly the northeastern part, while EM31-6k shows no obvious change over that region. A decrease in the Arctic SSS in 6k compared to preindustrial (Figures 3e and 3f) is revealed by both ECHAM6-MPIOM models with low and higher resolution. Moreover, because of the warming over Nordic
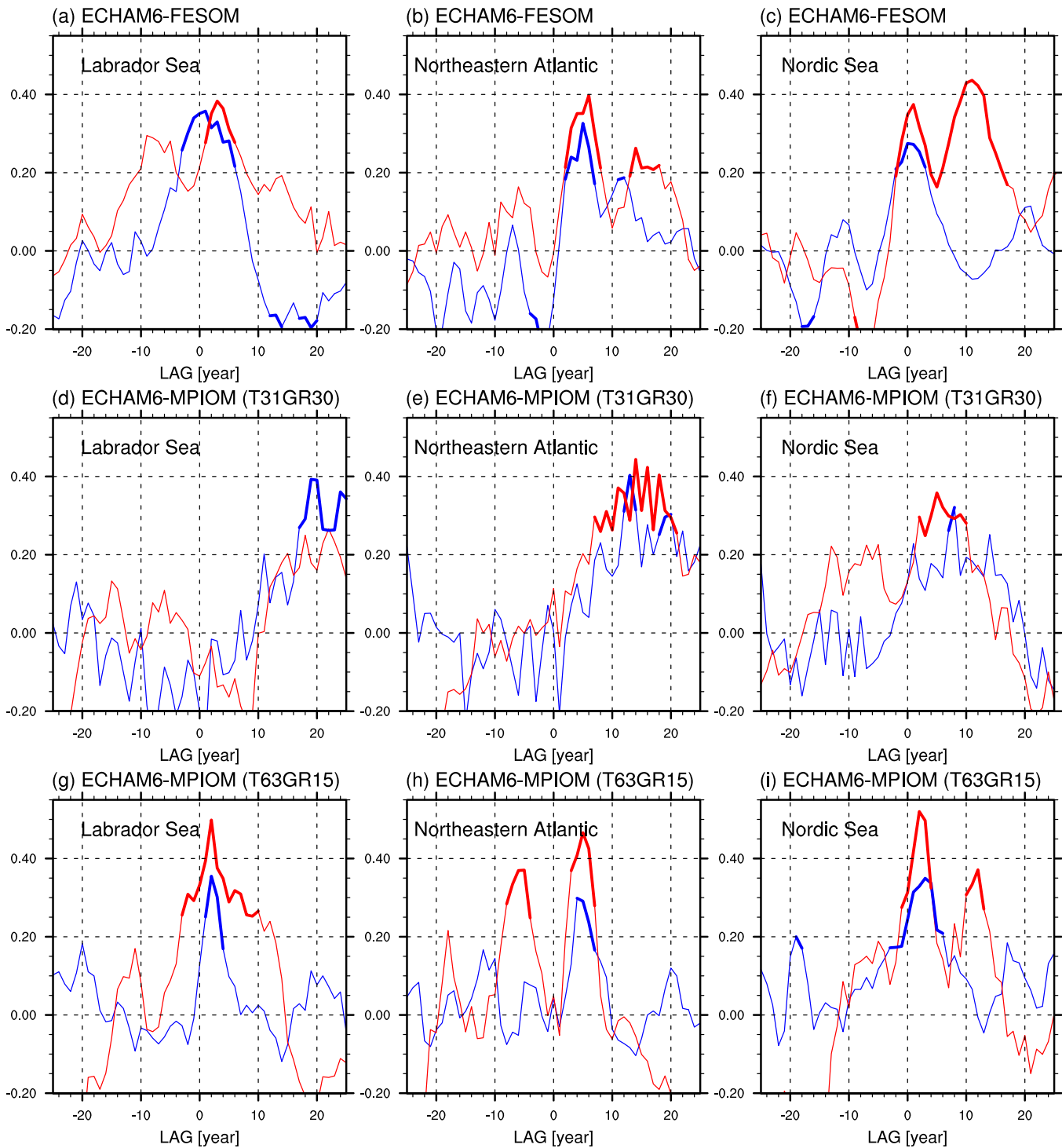
Figure 5. (a–c) Lag correlation coefficients between AMOC indices and averaged surface density over (a) Labrador Sea, (b) northeastern Atlantic, and (c) Nordic Sea in ECHAM6-FESOM. (d–f) As in Figures 5a–5c, but for ECHAM6-MPIOM (T31GR30). (g–i) As in Figures 5a–5c, but for ECHAM6-MPIOM (T63GR15). Blue lines are for preindustrial, and red lines for mid-Holocene. The AMOC indices are derived from the maximum meridional stream function at 500–2000 m depth and 30–50°N in the Atlantic Ocean. Taking into account the auto-correlation, thick segments indicate >97.5% significance level based on Pearson's R-test given N degrees of freedom, where N equals to the number of data points divided by 2 times e-folding time of auto-correlation [Leith, 1973]. Positive lags (yr) indicate that the density leads the AMOC and vice versa.

Sea in EM63-6k, the surface density in that region is significantly decreased, which is the opposite to the case for EF-6k. As the Nordic Sea is one of the main deep water formation sites, such change can contribute to a weakening of the thermohaline circulation in EM63-6k. However, the effect of increased density of

Labrador Sea dominates the change of the AMOC. However, different SSS patterns are simulated over the North Atlantic Ocean. In EM31-6k, the surface seawater of North Atlantic and Nodic Sea is significantly freshened, whereas EM63-6k presents an increase of about 0.3 psu in the salinity of the Greenland Sea and North Atlantic subpolar gyre, which is consistent with the result of ECHAM6-FESOM, even though smaller in magnitude. The density anomalies, similar to the SSS patterns in both models, present a less dense North Atlantic in EM31-6k, and the opposite case for EM63-6k (Figures 3h and 3i).

Deep convection in subpolar regions is the main driving mechanism for AMOC. As the deepest Northern Hemisphere mixed layer depth (MLD) happens in March, here we depict the distributions of March MLD in the three models (Figure 4). Identified by deep MLD, three main deep water formation sites simulated by the three models are located at (1) the Labrador Sea (shown in the red box of Figure 4), (2) the northeastern North Atlantic (blue box), and (3) the Nordic Sea (green box), in good agreement with observations and most climate models [*Danabasoglu et al.*, 2014]. However, the simulated MLD over northeastern Atlantic in ECHAM6-FESOM is not consistent with the observed deep convection area over Irminger Sea [*Pickart et al.*, 2003], but more toward the region between Iceland and Scotland. Differences in the modeled MLD are also noticed. For example, ECHAM6-FESOM depicts extreme MLD in the eastern North Atlantic. Deep convection in the Labrador Sea is much less pronounced, owing to an excessive simulated sea ice cover extending into the northwestern North Atlantic Ocean. ECHAM6-MPIOM with T63GR15 grid shows the deepest mixed layer at the Labrador Sea and Nordic Sea, while MLD of ECHAM6-MPIOM T31GR30 is deeper in the Nordic Sea than other regions. Besides, the deep water formation sites of the Labrador Sea and northeastern North Atlantic in ECHAM6-MPIOM T31GR30 are much smaller and shallower than in other two models.

The differences of simulated anomalies of MLD are shown in supporting information Figure S1. As can be seen, EF-6k and EM63-6k both reveal pronounced increase in MLD over Labrador Sea and the Nordic Sea compared to preindustrial conditions. In contrast, EM31-6k shows a thinner mixed layer over Nordic Sea. Moreover, no significant change is found over the Labrador Sea MLD in EM31-6k. Such MLD anomalies pattern as shown in supporting information Figure S1 indicates that both Labrador Sea and the Nordic Sea are important regions governing the AMOC difference between mid-Holocene and the present.

To further demonstrate the relationship between the North Atlantic density and AMOC, we define in the model three regions as shown in boxes in Figure 4, which cover the three deep water formation sites, respectively. We calculate the lag correlation coefficients between the AMOC indices and the averaged surface density over the respective deep MLD region as shown in Figure 5. For the Labrador Sea, the correlation coefficients reach the maximum with significant values when the density leads the AMOC by 1 and 3 years in EF-CTR and EF-6k, respectively. Coarse-resolution model ECHAM6-MPIOM show no obvious relationship between the Labrador density and the overturning circulation, even though a small coefficient value (<0.3) is found when density lagging the AMOC 18 years. This is might due to the relatively narrow and shallow MLD in EM31-CTR and EM31-6k. ECHAM6-MPIOM in T63GR15 shows the maximum correlation coefficients when the Labrador density leads the AMOC 2 years.

The density over the northeastern North Atlantic has a peak correlation with AMOC when leading about 6, 15, and 5 years in ECHAM6-FESOM, ECHAM6-MPIOM (T31GR30) and ECHAM6-MPIOM (T63GR15), respectively. Besides, another peak is as well detected by EM63-6k when the AMOC leads the density 5 years. This is reasonable, as a stronger AMOC brings more saline and dense seawater from the midlatitudes to the north, and causes a heat loss which provides for a Labrador Sea cooling. As the MLD of northeastern Atlantic is relatively shallower in ECHAM6-MPIOM in both grids compared to that of other deep water formation sites, we think that the high correlation between the surface density over the northeastern box and the AMOC might partly owing to seawater advection between that region and the Labrador Sea.

Two peak correlation coefficients are noticed in EF-6k, when the density over Nordic leads the AMOC indices 2 and 12 years. For EF-CTR, only one maximum value is found, with a lag of 1 year. In terms of ECHAM6-MPIOM, the coarse-resolution version shows the most maximum correlation value when the Nordic Sea density leads the AMOC 5–8 years, and the T63GR15 version indicates a lag of 2–4 years when the correlation coefficients reach the maximum.

Lag correlation coefficients between AMOC indices and averaged SSS over the deep MLD sites are similar to Figure 5 (not shown), as salinity is the most important contributor to seawater density. In summary, all

experiments show a clear response of the simulated AMOC to the averaged density/salinity over the main deep water formation sites, with a lag of varying years.

3.3. Atmospheric *Processes Rel*ated to AMOC
3.3.1. North Atlantic Oscillation (NAO)

There are a broad range of evidences, including observations and model simulations, suggest that the changes in the AMOC are likely to be the result of natural multidecadal climate variability and are driven by low-frequency variations of the NAO—a leading mode of natural atmospheric variability [*Hurrell*, 1995]—through changes in the deep convection of Labrador Sea [e.g., *Houghton*, 1996; *Dickson*, 1997; *Curry et al.*, 1998; *Eden and Willebrand*, 2001; *Latif et al.*, 2006; *Latif and Keenlyside*, 2011; *Scholz et al.*, 2014]. In this
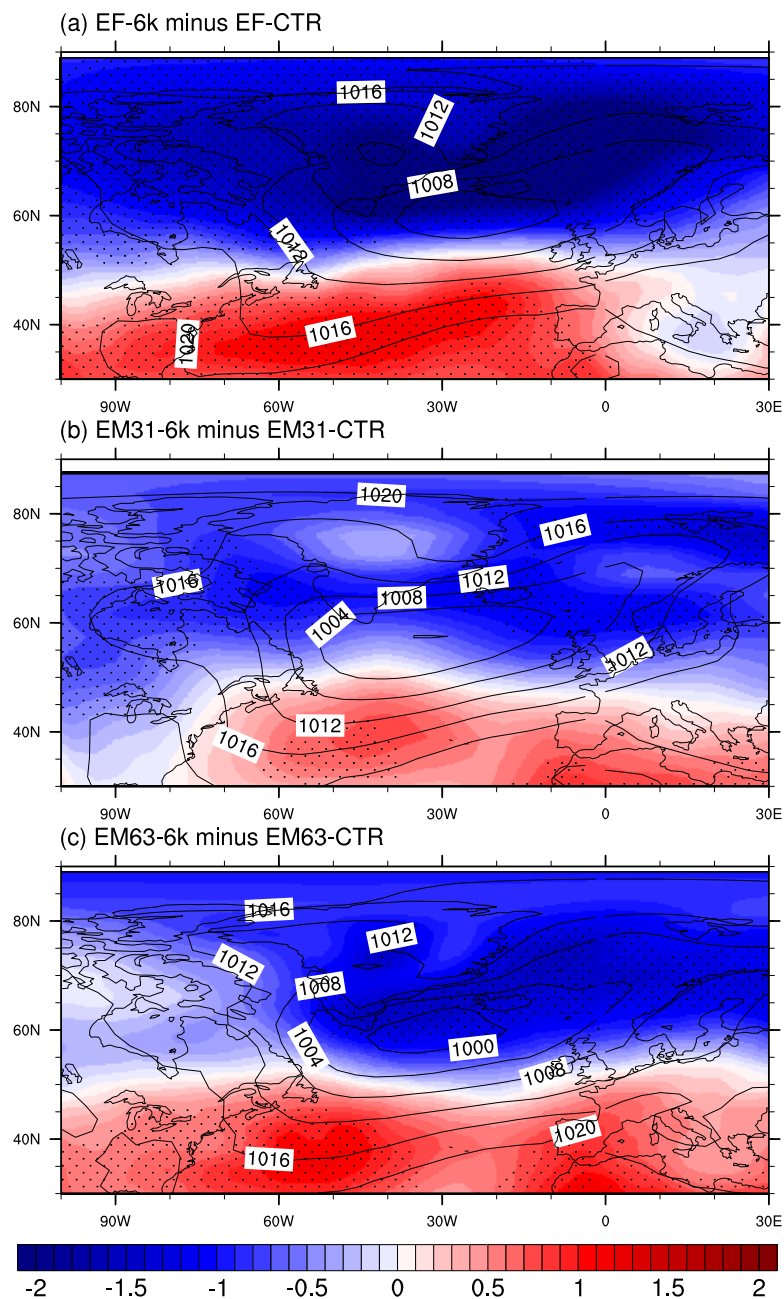

Figure 6. Simulated DJF SLP anomalies over the North Atlantic Ocean. Units are hPa. Coutour lines in each panel represent the corresponding absolute values in control experiment. Regions with >95% significance level (based on Student's *t*-test) are hatched by black dots.

section, we focus on the hydrological budget and convection state in the deep water formation sites, which is linked to the atmospheric NAO variability.

There is generally a consistent distribution in the December-to-February (DJF) anomalies in 6k mean sea level pressure (SLP) compared to preindustrial (Figure 6). Common features in the three models include a anomalous lower SLP north of 50°N centering at Iceland, a higher SLP south of 50°N, and a tendency toward an increased latitudinal gradient in mean SLP, forming a positive NAO-like mode.

The MLD over Labrador Sea and Nordic Sea has a fast response to the change of NAO in our simulations (not shown). The thicker MLD over Nordic Sea in EF-6k and EM63-6k can be attributed to the more positive phase of NAO in mid-Holocene. However, the response of Nordic Sea MLD to NAO in EM31-6k is the opposite, which shows a decreased MLD over that region during high NAO years. Such discrepancy is one important reason for the different MLD anomalies in the three models.
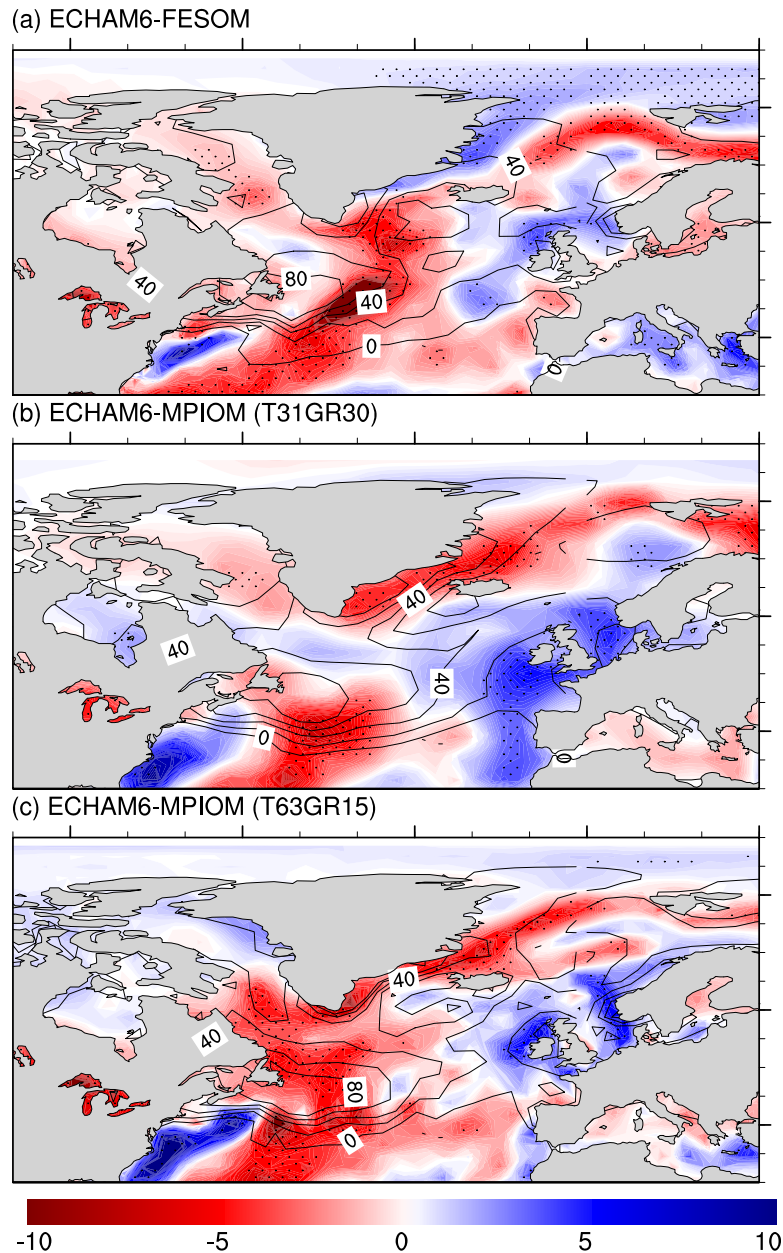

Figure 7. Simulated annual mean precipitation minus evaporation (P − E) anomalies over the North Atlantic Ocean. Units are mm/month. Coutour lines in each panel represent the corresponding absolute values in control experiment. Regions with >95% significance level (based on Student's T test) are hatched by black dots.

3.3.2. Net Precipitation

As depicted in Figure 7, the distribution of precipitation minus evaporation (P − E) anomalies is characterized by: (1) drier conditions over Baffin Bay, Nordic Sea, and western North Atlantic including the Labrador Sea; (2) wetter conditions over northeastern North Atlantic and the coastal region of America. One exception is that a local increased P − E is simulated by EM31-6k over a small part of the Labrador Sea, even though not significant.

The differences of P − E as illustrated in Figure 7 contribute to the SSS and density anomalies as in Figures 3d–3i. In detail, the saltier and denser Labrador Sea, North Atlantic subpolar gyre and Nordic Sea in EF-6k is partly owing to the reduced P − E over those regions. Similarly, EM63-6k produces a more dense seawater over Labrador Sea, North Atlantic subpolar gyre and Greenland Sea, which can be induced by the corresponding P − E anomalies distributions. In contrast, the wetter conditions over Labrador Sea and northeastern North Atlantic in EM31-6k contribute to a decreased salinity and density over the respective region.

The behaviors of the three models in terms of their P − E anomalies distributions in the Labrador Sea are associated with a response to the NAO Index variability (NAOI, not shown). In summary, the main difference in model behavior regarding the P − E anomalies (6k minus 0k) happens mainly over the Labrador Sea, which lies on the different P − E responses to NAO variability between low and higher resolution models. The composite maps of P − E in respect to high NAOI are shown in supporting information Figure S2. In good agreement with previous studies [e.g., *Hurrell*, 1995; *Hurrell et al.*, 2003] for present climate, evaporation exceeds precipitation over much of Baffin Bay and Labrador Sea during high NAOI years, one clear exception is in EM31-CTR, where net precipitation occurs in part of the Labrador Sea during high NAOI years, similar to the P − E anomalies pattern. Moreover, the responses of 6k P − E to the NAO indices show similar patterns (not shown here).

3.3.3. Surface Heat Fluxes

Figure 8 presents the surface heat flux changes between 6k and preindustrial runs. There is no obvious difference in conductive heat flux (CHF, positive downward) over the central Arctic Ocean (Figures 8a–8c), indicating no significant influence of sea ice change on CHF. Enhanced loss of conductive heat happens over Greenland and Barents Seas, which dominates the patterns of net surface heat flux (Figures 8g–8i). There is a general increase in net surface radiative flux (SRF, positive downward) for the whole Arctic region and Northern Hemisphere continents (Figures 8d–8f), dominating the enhanced total heat flux in the Arctic Ocean (Figures 8g–8i). Such SRF anomaly is mainly owing to the redistributed solar insolation in boreal summer, and to the reduction of the Arctic sea ice (i.e., ice-albedo feedback). The warming of Arctic SAT in 6k compared to preindustrial in ECHAM6-FESOM (not shown here) is mainly a result of enhanced net surface heat flux. A more pronounced feature of CHF and total heat flux in EF-CTR and EM63-CTR is the negative and positive anomalies over Northwestern Atlantic and Northeastern Atlantic, respectively, which is similar to the NAO-related heat flux distribution (supporting information Figures S3a and S3c). However, a reversed pattern is found for EM31-CTR (supporting information Figure S3b), which leads to an increased CHF and total heat flux over the Labrador Sea.

Ocean model simulations reveal that NAO-related net loss of surface heat flux over the Labrador Sea can induce a fast response (lag 2–3 years) of the AMOC [*Häkkinen*, 1999; *Eden and Willebrand*, 2001], through boundary wave processes which rapidly formed between subpolar and tropical latitudes[*Getzlaff et al.*, 2005]. Such mechanism is also detected on longer time scales [*Visbeck et al.*, 1998; *Latif et al.*, 2004]. Thus, we conclude that the simulated discrepancy in 6k AMOC in coarse and higher resolution models is likely owing to the different response of the Labrador Sea surface heat flux to NAO variations.

3.4. Oceanic *Processes Related* to AMOC
3.4.1. Growth/Melt of Sea Ice

Figure 9a depicts the change of annual mean sea ice thickness in the Arctic. Compared to EF-CTR, a notable feature in EF-6k is a significant decrease in sea ice thickness, coinciding with the increased boreal summer insolation. The maximum change is about −1 m on an annual average, occurring over the north of Greenland, this is simply a reflection of the increased advection of sea ice volume from the central Arctic by the Beaufort Gyre. Similarly, ECHAM6-MPIOM in both resolutions indicates a pronounced decrease in Arctic sea ice (Figures 9b and 9c), while the response is more pronounced in the coarse-resolution model.
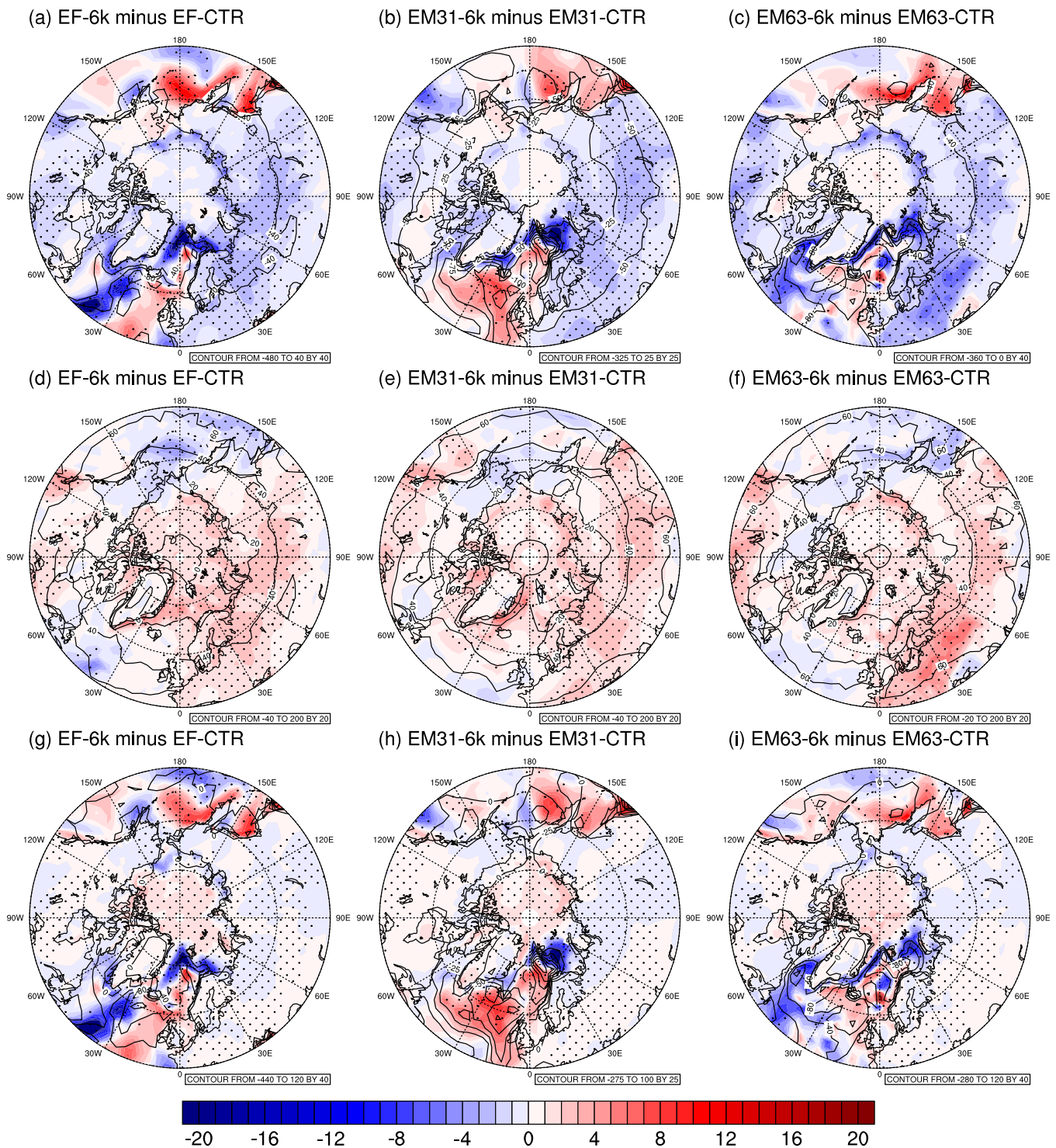
Figure 8. Simulated annual mean anomalies for (a–c) surface conductive heat flux, i.e., the sum of surface latent and sensible heat fluxes, (d–f) net surface radiative flux, i.e., the sum of net surface longwave and shortwave fluxes, and (g–i) net surface heat flux, i.e., the sum of surface conductive heat flux and net surface radiative flux. Blue means net heat loss, and red represents net heat gain. Units are W/m². Coutour lines in each panel represent the corresponding absolute values in control experiment. Regions with >95% significance level (based on Student's t-test) are hatched by black dots.

The freshened Arctic Ocean is led by the smaller net sea ice formation during mid-Holocene compared to present. Moreover, the coastal region of Greenland is found to be less dense in 6k, which is also a result of the reduced sea ice volume over there.
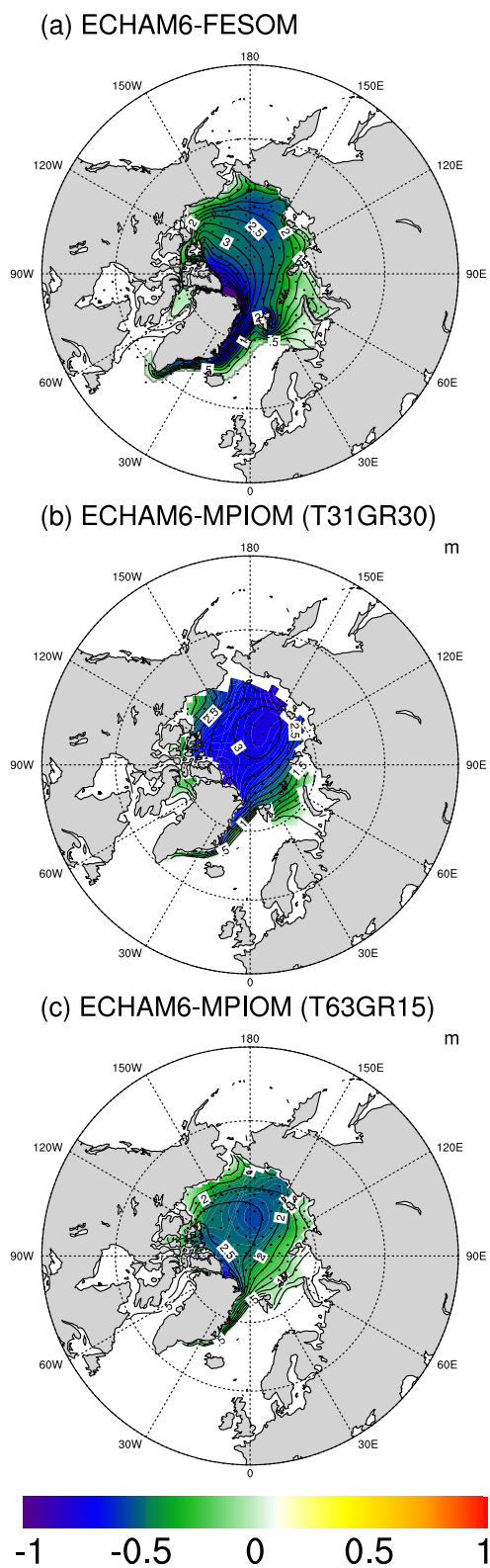
Figure 9. Simulated annual mean anomalies for the Arctic mean sea ice thickness. Units are m. Coutour lines in each panel represent the corresponding absolute values in control experiment. Regions with >95% significance level (based on Student's *t*-test) are hatched by black dots.

3.4.2. Transport of Sea Ice

In this section, we focus on the link of sea ice dynamics with density over the region of deep water formation. Multiyear sea ice originating in the Arctic Ocean is being exported through the Fram Strait into the Greenland Sea and represents a large amount of drain in the freshwater balance of the Arctic Ocean. As shown in Figure 9, less sea ice, associated with an increase in summer solar insolation, is simulated in our mid-Holocene experiments. Relating to the loss of sea ice in the Central Arctic Ocean, there is a reduction of sea ice volume import through Fram Strait (ICEFS) (Figures 10a–10c), with the annual mean anomaly being −0.016, −0.026, and −0.012 Sv for EF-6k, EM31-6k and EM63-6k, respectively, which is significant on 99% level. Such change results in a pronounced increase of salinity over the associated subpolar regions (Figures 3d–3i).

To further investigate the influence of the Fram Strait sea ice import on deep water formation, composite analyses are calculated as depicted in supporting information Figure S4, by averaging the density anomalies fields that have less than one standard deviation with respect to indices of ICEFS. It is noteworthy that such composite maps of density during low phase of ICEFS (supporting information Figure S4) are very similar to the distributions of density anomalies as shown in Figures 3g–3i. When small ICEFS occurs in EF-CTR, there is a pronounced increase in the density over subpolar North Atlantic Ocean and Greenland Sea with a delay of 2 years. Considering the regions of deep water formations (Figure 4) and the AMOC response to seawater density (Figure 5), we see that the reduction in Fram Strait sea ice import to lower latitudes in EF-6k causes an increase in density over deep water formations sites, further leading to a stronger deep water formation and hence a strengthening in AMOC.

Similar pattern is revealed by EM63-CTR except three specific features: (1) the values are of smaller magnitude, (2) the most pronounced response happens over 40°N–50°N, resembling the density anomalies (Figure 3i), and (3) no significant response of surface density is found to reduced ICEFS over the Labrador Sea deep water formation site, as the positive anomalies occur mainly along the Labrador Sea boundary current. Therefore, unlike EF-6k, there is no evidence for a link between the ICEFS and the Labrador Sea convection in EM63-6k. Thus, the increased MLD over the Labrador Sea is mainly a response to the atmospheric process, i.e., a more positive NAO phase in 6k compared to the present.
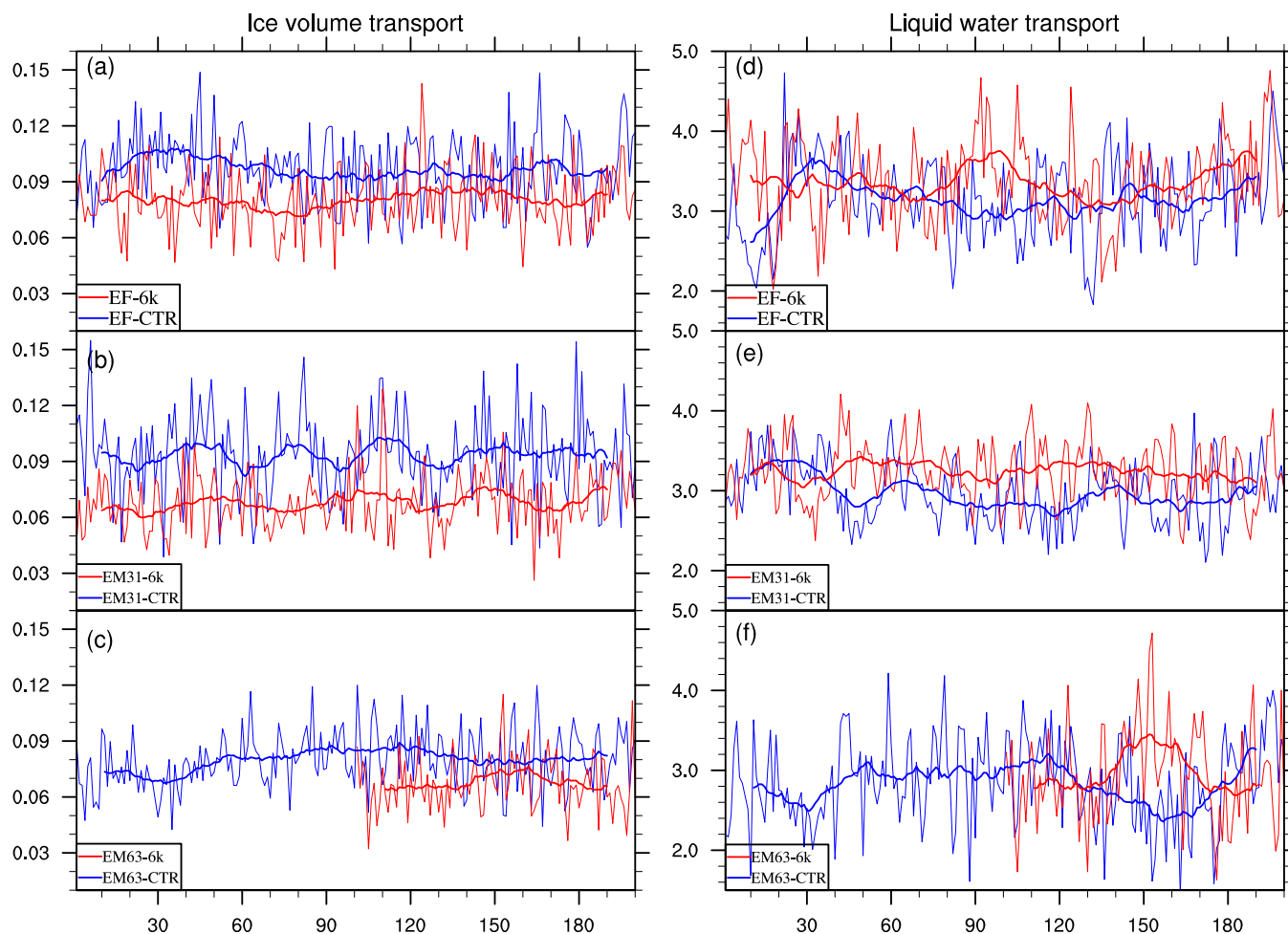
Figure 10. (a–c) Time series of sea ice volume transport through Fram Strait in (a) ECHAM6-FESOM, (b) ECHAM6-MPIOM in T31GR30 grid, and (c) ECHAM6-MPIOM in T63GR15 grid. For the thick lines, a 21 years filter is applied. Units are Sv. (d–f) As in Figures 10a–10c, but for seawater volume transport through the Fram Strait. Units are Sv.

In contrast, EM31-CTR indicates increased density over the Labrador Sea and coast of Greenland when led 1 year by low ICEFS, while other regions (e.g., northeastern North Atlantic) experience a general decrease in seawater density (supporting information Figure S4). However, the seawater over south of Greenland is freshened by larger seawater import from the Arctic and slight (not significant) increased P − E, which compensates the influence of reduced sea ice transport. Therefore, the combined effect of these process-es leads to the density anomalies as in Figure 3h. The weakened AMOC in EM31-6k is a consequence of the diluted Nordic Sea and northeastern North Atlantic (Figure 3h).

The composite maps between density anomalies and low ICEFS in the mid-Holocene experiments are simi-lar to supporting information Figure S4, therefore is not shown here.

3.4.3. Transport of Seawater
Ocean current is one of the main causes for density advection. From the north, the North Atlantic exchanges seawater with the Arctic Ocean through the Canadian Archipelago, Fram Strait, and Barents Sea Opening. From the south, the warmer and saltier water mass flows into the North Atlantic Ocean, which forms the upper branch of meridional overturning circulation.

Here we focus on the liquid water volume import through Fram Strait (LWFS) in the three models, as no significant differences are found for the transport of Arctic seawater through Canadian Archipelago and Barents Opening. Figures 10d–10f illustrate the time series of annual mean LWFS, it can be seen that all mid-Holocene experiments tend to simulate larger amount of LWFS than their preindustrial counterparts, with the averaged difference being 0.24 Sv (significance level >99%), 0.27 Sv (>99%), and 0.1 Sv (90%) in
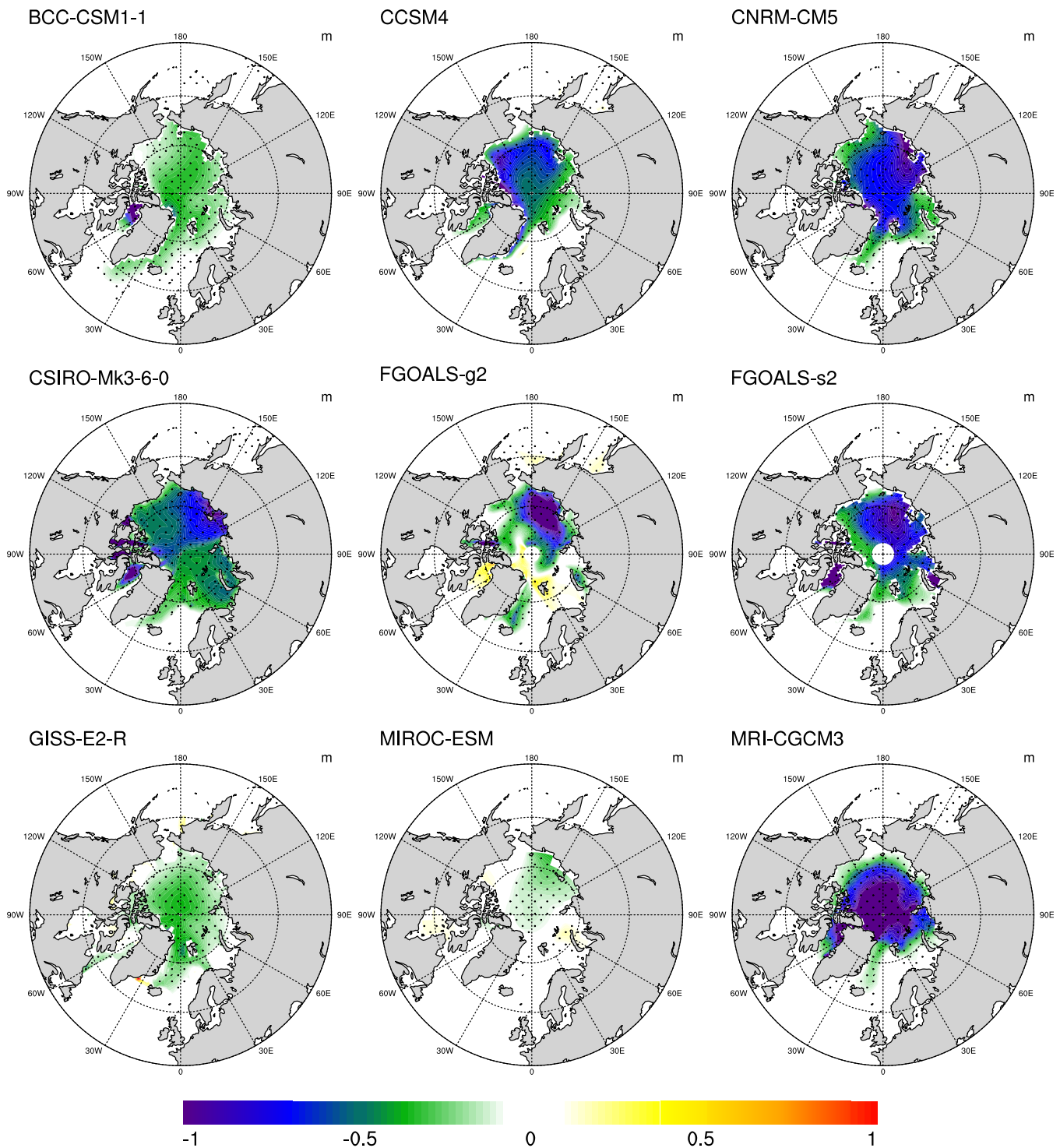
Figure 11. Simulated annual mean ice thickness anomalies in different models. Units are m.

ECHAM6-FESOM, ECHAM6-MPIOM (T31GR30), and ECHAM6-MPIOM (T63GR15), respectively. The positive anomalies in LWFS contribute to a freshening Greenland Sea and Labrador Sea (supporting information Figure S5). For EM31-CTR, such freshening mainly occurs at the northeastern Atlantic Ocean (supporting information Figure S5b).
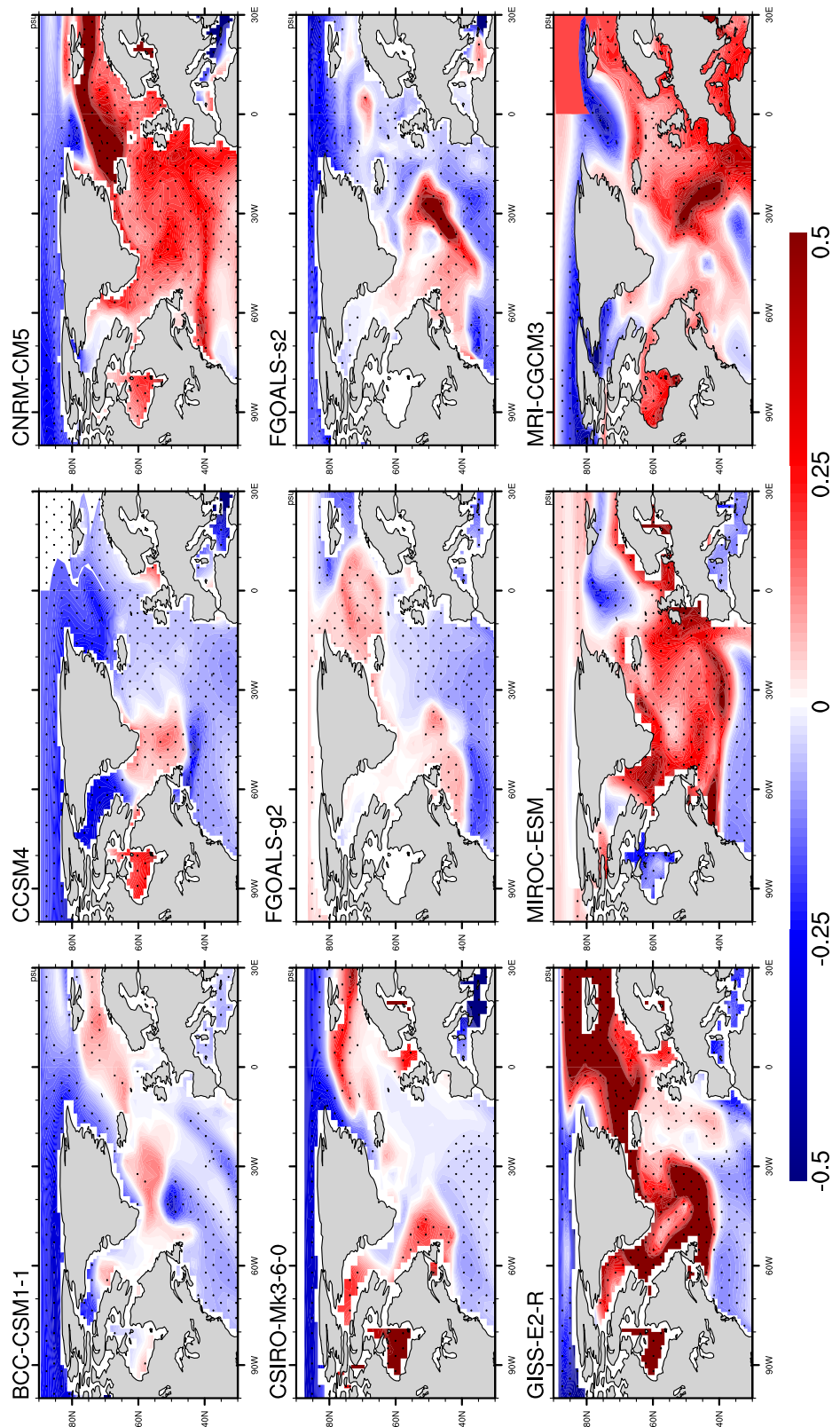
Figure 12. Simulated annual mean sea surface salinity anomalies in different models. Units are psu.
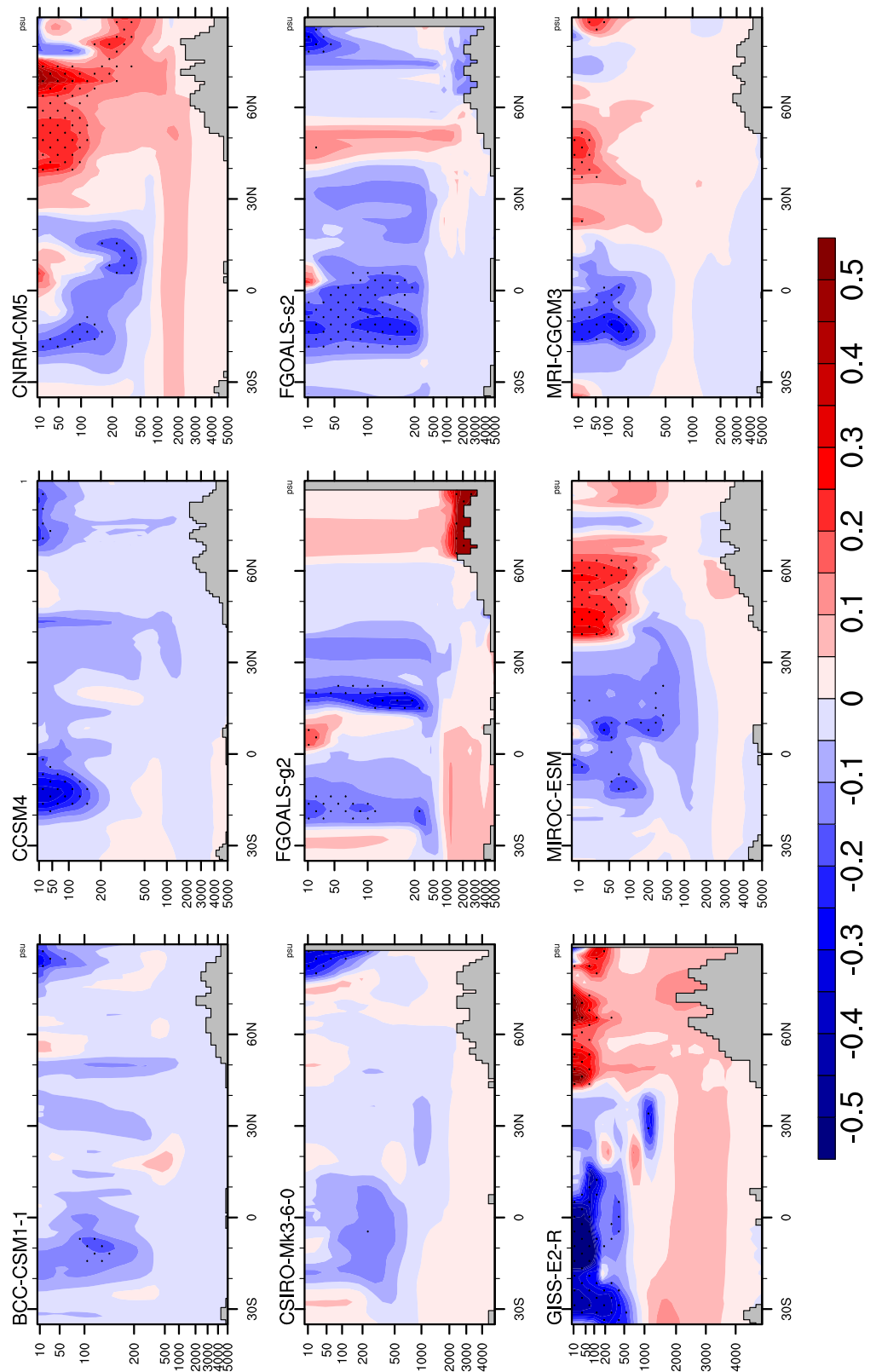
Figure 13. Simulated annual mean ocean salinity anomalies for the Atlantic region in different models. Units are psu.
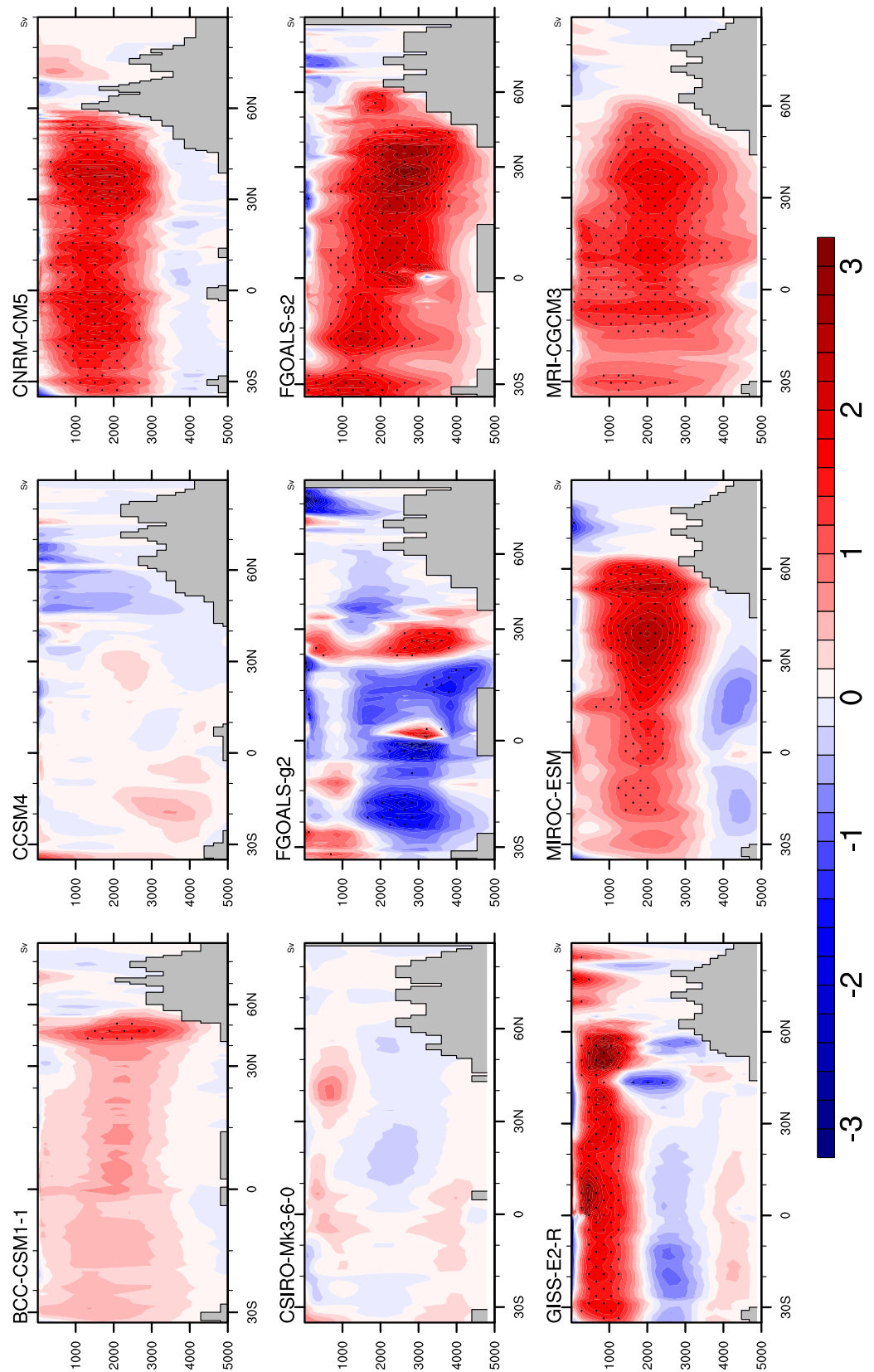
Figure 14. Simulated AMOC anomalies in different models. Units are Sv.

With enhanced AMOC, the relatively warmer and saltier seawater which origins from lower latitudes advects to the North Atlantic Ocean. The AMOC response in turn generates positive salinity (and density) anomalies. This well-known salinity-advection mechanism is a positive feedback on the thermohaline circulation response [*Stommel*, 1961]. Therefore, the positive/negative salinity anomalies in the North Atlantic simulated in different models is partly a consequence of the change in AMOC strength.

3.5. Results of Other Coupled Climate Models

The simulated AMOC may differ from model to model, here we have a supplementary analysis of the climatology data of different models from CMIP5 [*Taylor et al.*, 2012] (Table 2) to have a further view of the AMOC change.

Figure 11 depicts the annual mean sea ice thickness anomalies in different models (cf., Figure 9). Most of the models represent an obvious decrease in the sea ice thickness. FGOALS-g2 show a general decrease in sea ice but in some parts of the Arctic, for example, regions to the north and west of Greenland, and in the western Barents Sea, thicker sea ice is found. MIROC-ESM also simulates increased ice in some regions, but at a smaller magnitude.

The SSS anomalies in different CMIP5 models, as well as the main three models used in this study, are depicted in Figure 12 (cf., Figures 3d–3f). BCC-CSM1-1, CCSM4, CSIRO-Mk3-6-0, and FGOALS-s2 simulate fresher seawater in the whole Arctic. FGOALS-g2 shows no obvious change in SSS over midlatitudes and high latitudes. MIROC-ESM presents a maximum change of about 0.5 psu in the Northern Atlantic Ocean, but no significant change in the Central Arctic. There are three models (i.e., CNRM-CM5, GISS-E2-R, and MRI-CGCM3) show decreased salinity in the Central Arctic and increased SSS over the GIN Sea and North Atlantic subpolar region.

The meridional profiles of ocean salinity in CNRM-CM5, GISS-E2-R, MIROC-ESM, and MRI-CGCM3 are similar to ECHAM6-FESOM and ECHAM6-MPIOM (T63GR15) (Figure 13, cf., supporting information Figure S6), with denser and fresher seawater over the northern and southern Atlantic, respectively. ECHAM6-MPIOM (T31GR30) indicates the opposite pattern. Besides, BCC-CSM1-1, CCSM4, CSIRO-Mk3-6-0, FGOALS-s2, and FGOALS-g2 show a general decrease in ocean salinity.

Owing to the salinity anomalies of seawater in CNRM-CM5, GISS-E2-R, MRI-CGCM3, and MIROC-ESM, the associated AMOC is enhanced in these models (Figure 14, cf., Figure 2). FGOALS illustrates different results in its two versions, as weakened AMOC is presented in FGOALS-g2 and stronger AMOC in FGOALS-s2, which is in agreement with *Zheng and Yu* [2013]. There is only a slight change of AMOC in BCC-CSM-1, CCSM4, and CSIRO-Mk3-6-0.

4. Discussion

The ice-ocean component in FESOM has the advantage in the ability to provide a regional focus in an otherwise global setup [*Sidorenko et al.*, 2011]. In our paper, FESOM applies even higher resolution in the high latitudes, is therefore suitable for investigating polar properties particularly sea ice characteristics.

Simulations by ECHAM6-FESOM show an increase of 1–2 Sv in mid-Holocene AMOC compared to the preindustrial state, and the position of the maximum AMOC shifts northward. Such northward displacement is likely linked to the crossover between the equatorward deep western boundary current and the northward Gulf Stream [e.g., *Kwon and Frankignoul*, 2014]. In contrast, some former studies [e.g., *Ganopolski et al.*, 1998; *Otto-Bliesner et al.*, 2006; *Fischer and Jungclaus*, 2010; *Wei and Lohmann*, 2012], show a weakened AMOC in the mid-Holocene compared to that of the preindustrial. The main reason for this inconsistency in AMOC change between our results and those others, lies on the different ocean salinity patterns simulated over the North Atlantic Ocean. The past studies show an decrease in ocean salinity in the upper layer of the North Atlantic Ocean, causing a decrease in water mass density in the deep water formation sites, while our simulations indicate an increase in the water salinity/density over the regions of deep mixed layer owing to a change of precipitation minus evaporation which is linked to a tendency of positive NAO mode, and to a sea ice dynamic process, namely, the decreased import of sea ice from the Arctic reduces the incoming fresh water to the Greenland Sea and Nordic Sea. In addition, by performing model simulation with mid-

Holocene setup, *Rimbu et al.* [2003]; *Lohmann* [2016] associate such NAO tendency with tropical warming during winter induced by increasing in solar insolation, similar to our results.

The main three models used in the present study all produce a tendency towards a positive NAO state in 6k, however, the response of Labrador Sea P − E to the NAO+ mode in ECHAM6-MPIOM (T31GR30) is opposite to that in other models, as precipitation exceeds evaporation happens in ECHAM6-MPIOM with T31GR30 grid, and the higher resolution models (i.e., ECHAM6-MPIOM (T63GR15) and ECHAM6-FESOM) show the opposite case. There are clear indications that the North Atlantic Ocean varies significantly with the overlaying atmosphere, in particular the NAO [*Visbeck et al.*, 2003; *Scholz et al.*, 2014]. *Curry et al.* [1998] indicate that NAO variability has an influence on deep convection in the Labrador Sea. Changes in the mean circulation patterns over North Atlantic associated with NAO are companied by changes in the intensity and number of storms, which are reflected in pronounced changes in the transport and convergence of atmospheric moisture and hence the P − E distribution [*Hurrell*, 1995; *Dickson et al.*, 2000]. In this paper, we argue that the NAO-induced P − E change leads to a response in the North Atlantic hydrological budget and further affects the overturning circulation. By ocean model simulations, *Häkkinen* [1999]; *Eden and Willebrand* [2001] suggest that NAO-related variations in the Labrador Sea heat flux induce a fast response of the AMOC, with a delay of 2–3 years. Based on analyses of ocean observations and model simulations, *Latif et al.* [2006] conclude that the changes in the thermohaline circulation during last century is driven by low-frequency variations of NAO through changes in Labrador Sea convection. More recently, a delayed oscillator model suggests that NAO forces AMOC on a 60 year cycle [*Sun et al.*, 2015; *Scholz et al.*, 2014].

Until recently, some (very sparse) efforts have been made to reconstruct the NAO and AMOC of mid-Holocene. For example, paleoenvironmental proxy data suggest a prominent role of NAO-like atmospheric variability during the Holocene beyond interannual to interdecadal time scales [*Lamy et al.*, 2006], which is attributed to the solar forcing. Using temperatures reconstructed from pollen data *Davis et al.* [2003] suggest a strongly negative NAO regime during the early Holocene (9–12 ky BP) rising to a slightly positive NAO regime during the mid-Holocene, then decreasing to preindustrial NAO. According to the ratio of Pa/Th, *McManus et al.* [2004] shows a brief decline in meridional overturning circulation from the mid-Holocene to 3000 years ago, and the AMOC at 6k and at present are of similar magnitudes. But there is uncertainty in the interpretation of AMOC by Pa/Th [*Keigwin and Boyle*, 2008], and a subsequent set of Pa/Th records suggested that a complete AMOC cessation during HS1 (Heinrich stadial event 1) was unlikely [*Gherardi et al.*, 2009]. The paleo reconstructions indicate that the uncertainties in the proxies data need to be reduced significantly to come to a final data-based conclusion about the past AMOC conditions [e.g., *Huybers et al.*, 2007; *Burke et al.*, 2011]. Moreover, there are reconstruction records suggesting an increase of ocean salinity over the North Atlantic Ocean [e.g., *de Vernal and Hillaire-Marcel*, 2006; *Came et al.*, 2007]. However, these reconstructions are based on a simple relationship between salinity and $\delta^{18}O$, which is an under-debate assumption [e.g., *Xu et al.*, 2013]. More recently, *Thornalley et al.* [2009] and *Rasmussen and Thomsen* [2010] show a slight decrease in North Atlantic salinity in 6k compared to the present. Based on the discrepancy of the reconstructed salinity, we discuss here that so far there is no robust conclusion for the 6k salinity change over North Atlantic. A better indicator might be the significant warming over the Gulf Stream, as observed by proxy data [*Lohmann et al.*, 2013], the 6k warming over the Gulf Stream is more pronounced than other regions in the North Atlantic Ocean. One can expect that with enhanced AMOC, the associated northward transport of the relatively warmer and saltier seawater, largely increases the temperature and salinity over the region of Gulf Stream, where the maximum SST gradient occurs. Such interpretation is agreed by *Latif et al.* [2004] who uses the dipole SST anomaly pattern as a fingerprint to detect change in the North Atlantic thermohaline circulation.

The simulated AMOC anomalies are affected by changes in P − E, surface heat flux, sea ice growth/melt, transport of sea ice, and liquid seawater from the Arctic, and the salinity-advection feedback related to AMOC itself. Here we propose a positive feedback between the Arctic sea ice and AMOC. The high phase of AMOC is found correlated to the increasing Northern Hemisphere surface air temperature (SAT) by numerous studies [e.g., *Schlesinger and Ramankutty*, 1994; *Rühlemann et al.*, 2004; *Knight et al.*, 2005; *Dima and Lohmann*, 2007; *Zhang*, 2007, 2008; *Chylek et al.*, 2009; *Mahajan et al.*, 2011; *Zhang*, 2015] by transferring advective heat flux into the Arctic interior through Fram Strait and the northern boundary of Barents Sea and Kara Sea. Therefore, the decreased mid-Holocene sea ice, can be both a cause and consequence of the enhanced AMOC. Moreover, the advective heat flux from the North Atlantic to the Arctic interior is found to

be primarily confined to the Atlantic water, which is below the shallow mixed layer and the Arctic halocline in the Arctic basin, limiting the direct contact between ocean and atmosphere [e.g., *Steele and Boyd*, 1998]. Modeling studies suggest that multidecadal variability in the AMOC strongly affects sea ice in the Arctic and particularly in the Barents Sea [*Delworth et al.*, 1997; *Jungclaus et al.*, 2005]. All of the three models used in this study exhibits sea ice reduction in the Barents Sea, however, only T63-versions show a positive AMOC response. Therefore, the AMOC-sea ice-SAT feedback is not conclusive in the simulations analyzed in the present paper. Besides, a similar temperature-sea ice-AMOC positive feedback has been also identified in hosing experiments in the North Atlantic Ocean [*Lohmann and Gerdes*, 1998], but without sea ice transport.

Another important component contributing to the positive feedback is the Fram Strait sea ice import into the GIN Sea. As a transition zone with no sea ice in the south and permanent ice cover in the north, the GIN Sea is a very important area in regulating the air-ocean interactions and heat exchange in horizontal direction. *Koenigk et al.* [2009] found that the interannual variability of sea ice volume in such transition region is mainly determined by variations in sea ice import from the Central Arctic, which is governed by local winds, and dynamic process for sea ice growth/melt is of minor importance compared to dynamic sea ice transport. This finding to a certain degree coincides with our result, which reveals that the freshwater budget in the subpolar region depends on the Arctic sea ice/freshwater transport, and the local radiation induced sea ice change plays a secondary role on the subpolar freshwater budget. The Fram Strait sea ice and water volume transport is sensitive to the atmospheric circulation in particular the surface wind over the Arctic Ocean [*Proshutinsky et al.*, 2015]. However, we observe no significant change in the surface wind and surface wind stress, therefore the reduction in sea ice volume import is mainly a consequence of the reduced Arctic sea ice. Analyzing paleoclimate data, *Müller et al.* [2009] conclude that changes in sea ice conditions in the Norwegian Sea are linked to regional and global climate anomalies and oceanographic circulation in the North Atlantic. A proper representation of these processes is therefore essential for simulating the climate response to external forcing.

AMOC is mostly driven by the sinking of dense water masses in high latitudes which form in marginal seas and slide down the continental slopes. One particular focus arises as to how important is the near-bottom overflow—dense near-bottom waters crossing sills between ocean basins. *Danabasoglu et al.* [2010] introduce a new overflow parameterization (OFP) of density-driven flows through ocean ridges via narrow, unresolved channels in CCSM4, which produces improved North Atlantic Deep Water (NADW) penetration depth and strength of AMOC. There are other model studies emphasizing the importance of overflow on the simulated AMOC [e.g., *Döscher and Redler*, 1997; *Lohmann*, 1998; *Yeager and Danabasoglu*, 2012]. However, there is no overflow parameterization in ECHAM6-FESOM, therefore the deep exchange from the Nordic Sea into the subpolar North Atlantic might be limited [*Danabasoglu et al.*, 2010]. As a consequence, the AMOC in ECHAM6-FESOM can be weaker and shallower compared to most other coupled climate model including ECHAM6-MPIOM [e.g., *Danabasoglu et al.*, 2014]. Another reason of the simulated weak AMOC lies on the freezing of parts of the Labrador Sea, limiting the deep convection there. Vice versa, the simulated excessive sea ice over the Labrador Sea is also a result of the weak AMOC. Future work is needed for an implementation of subpolar overflow parameterization in ECHAM6-FESOM. One expectation is that, with better treatment to the overflow phenomenon, the simulated AMOC and sea ice will be improved, therefore allowing a stronger deep convection over the Labrador Sea. Considering the significant positive density anomalies over the Labrador Sea, the simulated AMOC difference could be even more pronounced.

Most CMIP5 models, as discussed in section 3.5, show an enhanced AMOC in the mid-Holocene compared to present, in line with the result of ECHAM6-FESOM, but very few of them has been analyzed in previous studies [e.g., *Fischer and Jungclaus*, 2010; *Wei and Lohmann*, 2012; *Zheng and Yu*, 2013]. Results show a clear relationship between AMOC and SSS, as well as the vertical salinity profile. However, it is noted that the CMIP5 models show no obvious relationship with resolutions. In this paper, we focus on the behavior of ECHAM6-FESOM, and ECHAM6-MPIOM in different resolutions. Therefore, exploring the specific mechanism for mid-Holocene AMOC change in other CMIP5 models is beyond the scope of this study.

Model resolution is an important element in climate models. Our results show opposite AMOC responses to mid-Holocene regime in ECHAM6-FESOM/MPIOM with different resolutions. However, the dynamical mechanism controlling such discrepancy still needs further investigation. Moreover, the role of resolution might be model-dependent, as the CMIP5 models reveal very different AMOC responses even though with similar

resolution. To achieve a comprehensive conclusion, more analysis of other model results with different resolutions is needed.

5. Conclusions

In the present paper, the climate conditions of the mid-Holocene and preindustrial are simulated and compared. In good agreement with past studies [e.g., *Berger*, 1978; *Fischer and Jungclaus*, 2010; *Wei and Lohmann*, 2012; *Zheng and Yu*, 2013], we observe reduced sea ice and increased sea surface temperature in the polar regions, mainly induced by an increase in boreal summer solar insolation in 6k. However, we detect big discrepancies of simulated AMOC anomalies between models with coarse and higher resolutions. In detail, ECHAM6-FESOM and ECHAM6-MPIOM (T63GR15) both reveal a stronger-than-present AMOC in mid-Holocene, while ECHAM6-MPIOM T31GR30 shows the opposite case. Such model behavior lies on the different simulated salinity/density anomalies over the deep water formation sites, as the coarse-resolution model (ECHAM6-MPIOM T31GR30) produces a freshening/less dense Nordic Sea and most part of the North Atlantic Ocean, while other two higher-resolution models depict pronounced salinification over the North Atlantic in particular the Labrador Sea, and the Greenland Sea. In addition, an earlier version of ECHAM6-MPIOM with T31GR30 grid (COSMOS, i.e., ECHAM5-MPIOM) shows very similar results to ECHAM5-MPIOM T31GR30 [*Fischer and Jungclaus*, 2010; *Wei and Lohmann*, 2012]. We thus conclude that the simulated AMOC response is closely related to model resolution in these models.

The reason for such discrepancy in simulated AMOC anomaly (6k minus 0k) in ECHAM6-FESOM/MPIOM with different resolution is associated with both atmospheric and oceanic processes: first of all, all models produce a tendency toward a positive NAO state in 6k, however, the response of Nordic Sea deep convection, Labrador Sea P − E and surface heat flux to the NAO+ mode in ECHAM6-MPIOM (T31GR30) is opposite to that in other models, as thinner MLD over Nordic Sea, positive P − E and net heat flux anomalies over the Labrador Sea happen in ECHAM6-MPIOM with T31GR30 grid, and the T63 models show the opposite case. Second, all models produce a reduction in Fram Strait sea ice mass export, however, unlike other two models, the salinification induced by the reduced sea ice transport in ECHAM6-MPIOM (T31GR30) only occurs over a small region in the Labrador Sea, and is partly compensated by the increased P − E over there. Finally, the coarse-resolution model simulates much larger import of relatively fresh seawater from the Arctic to lower latitudes through Fram Strait in mid-Holocene compared to preindustrial, whereas such anomaly in ECHAM6-MPIOM (T63GR15) is not significant.

Other CMIP5 models, although have approximately similar resolutions, show very different response of the AMOC to 6k boundary conditions. However, exploring the nature of such association in every specific CMIP5 model is beyond the scope of this study. A logical next step would be the comparison of CMIP5 model scenarios with different resolution to identify the resolution-dependent mechanisms for the Holocene AMOC change, and to identify which resolution is the key influencing factor—the atmospheric resolution, the oceanic resolution, or both.

References

Bao, Q., et al. (2013), The flexible global ocean-atmosphere-land system model, spectral version 2: FGOALS-s2, *Adv. Atmos. Sci.*, *30*, 561–576.

Berger, A. (1978), Long-term variations of daily insolation and Quaternary climatic changes, *J. Atmos. Sci.*, *35*(12), 2362–2367.

Boville, B. A. (1991), Sensitivity of simulated climate to model resolution, *J. Clim.*, *4*(5), 469–485.

Braconnot, P., et al. (2007), Results of PMIP2 coupled simulations of the Mid-Holocene and Last Glacial Maximum—Part 1: Experiments and large-scale features, *Clim. Past*, *3*(2), 261–277.

Buizza, R., T. Petroliagis, T. Palmer, J. Barkmeijer, M. Hamrud, A. Hollingsworth, A. Simmons, and N. Wedi (1998), Impact of model resolution and ensemble size on the performance of an ensemble prediction system, *Q. J. R. Meteorol. Soc.*, *124*(550), 1935–1960.

Burke, A., O. Marchal, L. I. Bradtmiller, J. F. McManus, and R. François (2011), Application of an inverse method to interpret 231pa/230th observations from marine sediments, *Paleoceanography*, *26*, PA1212, doi:10.1029/2010PA002022.

Came, R. E., D. W. Oppo, and J. F. McManus (2007), Amplitude and timing of temperature and salinity variability in the subpolar North Atlantic over the past 10 ky, *Geology*, *35*(4), 315–318.

Chylek, P., C. Folland, G. Lesins, M. Dubey, and M. Wang (2009), Arctic air temperature change amplification and the Atlantic multidecadal oscillation, *Geophys. Res. Lett.*, *36*, L14801, doi:10.1029/2009GL038777.

Clement, A., K. Bellomo, L. N. Murphy, M. A. Cane, T. Mauritsen, G. Rädel, and B. Stevens (2015), The Atlantic Multidecadal Oscillation without a role for ocean circulation, *Science*, *350*(6258), 320–324.

Collier, M., et al. (2011), The CSIRO-Mk3. 6.0 Atmosphere-Ocean GCM: Participation in CMIP5 and data publication, in *International Congress on Modelling and Simulation–MODSIM*, 19th International Congress on Modelling and Simulation, Perth, Australia.

Crucifix, M., P. Braconnot, S. Harrison, and B. Otto-Bliesner (2005), Second phase of paleoclimate modelling intercomparison project, *Eos Trans. AGU*, *86*(28), 264–264.

Curry, R. G., M. S. McCartney, and T. M. Joyce (1998), Oceanic transport of subpolar climate signals to mid-depth subtropical waters, *Nature*, *391*(6667), 575–577.

Danabasoglu, G., W. G. Large, and B. P. Briegleb (2010), Climate impacts of parameterized nordic sea overflows, *J. Geophys. Res.*, *115*, C11005, doi:10.1029/2010JC006243.

Danabasoglu, G., et al. (2014), North Atlantic simulations in coordinated ocean-ice reference experiments phase ii (core-ii). Part i: Mean states, *Ocean Modell.*, *73*, 76–107.

Danilov, S., G. Kivman, and J. Schröter (2004), A finite element ocean model: Principles and evaluation, *Ocean Modell.*, *6*, 125–150.

Davis, B., S. Brewer, A. Stevenson, and J. Guiot (2003), The temperature of Europe during the Holocene reconstructed from pollen data, *Quat. Sci. Rev.*, *22*(15), 1701–1716.

de Vernal, A., and C. Hillaire-Marcel (2006), Provincialism in trends and high frequency changes in the northwest North Atlantic during the Holocene, *Global Planet. Change*, *54*(3), 263–290.

Delworth, T. L., S. Manabe, and R. J. Stouffer (1997), Multidecadal climate variability in the Greenland sea and surrounding regions: A coupled model simulation, *Geophys. Res. Lett.*, *24*(3), 257–260.

Dickson, B. (1997), From the Labrador sea to global change, *Nature*, *386*, 649–650.

Dickson, R., T. Osborn, J. Hurrell, J. Meincke, J. Blindheim, B. Adlandsvik, T. Vinje, G. Alekseev, and W. Maslowski (2000), The arctic ocean response to the north Atlantic oscillation, *J. Clim.*, *13*(15), 2671–2696.

Dima, M., and G. Lohmann (2007), A hemispheric mechanism for the Atlantic Multidecadal Oscillation, *J. Clim.*, *20*(11), 2706–2719.

Döscher, R., and R. Redler (1997), The relative importance of northern overflow and subpolar deep convection for the north Atlantic thermohaline circulation, *J. Phys. Oceanogr.*, *27*(9), 1894–1902.

Eden, C., and J. Willebrand (2001), Mechanism of interannual to decadal variability of the north Atlantic circulation, *J. Clim.*, *14*(10), 2266–2280.

Fischer, N., and J. Jungclaus (2010), Effects of orbital forcing on atmosphere and ocean heat transports in Holocene and Eemian climate simulations with a comprehensive Earth system model, *Clim. Past*, *6*(25), 155–168.

Ganachaud, A., and C. Wunsch (2000), Improved estimates of global ocean circulation, heat transport and mixing from hydrographic data, *Nature*, *408*(6811), 453–457.

Ganopolski, A., C. Kubatzki, M. Claussen, V. Brovkin, and V. Petoukhov (1998), The influence of vegetation-atmosphere-ocean interaction on climate during the mid-Holocene, *Science*, *280*(5371), 1916–1919.

Gent, P. R., et al. (2011), The community climate system model version 4, *J. Clim.*, *24*(19), 4973–4991.

Getzlaff, J., C. W. Böning, C. Eden, and A. Biastoch (2005), Signal propagation related to the north Atlantic overturning, *Geophys Res. Lett.*, *32*, L09602, doi:10.1029/2004GL021002.

Gherardi, J.-M., L. Labeyrie, S. Nave, R. Francois, J. F. McManus, and E. Cortijo (2009), Glacial-interglacial circulation changes inferred from 231pa/230th sedimentary record in the north Atlantic region, *Paleoceanography*, *24*, PA2204, doi:10.1029/2008PA001696.

Häkkinen, S. (1999), Variability of the simulated meridional heat transport in the north Atlantic for the period 1951–1993, *J. Geophys. Res.*, *104*(C5), 10,991–11,007.

Houghton, R. (1996), Subsurface quasi-decadal fluctuations in the north Atlantic, *J. Clim.*, *9*(6), 1363–1373.

Hunke, E., and J. Dukowicz (1997), An elastic-viscous-plastic model for sea ice dynamics, *J. Phys. Oceanogr.*, *27*, 1849–1868.

Hurrell, J. W. (1995), Decadal trends in the north Atlantic oscillation: Regional temperatures and precipitation, *Science*, *269*(5224), 676–679.

Hurrell, J. W., Y. Kushnir, G. Ottersen, and M. Visbeck (2003), An overview of the North Atlantic Oscillation, in *The North Atlantic Oscillation: Climatic Significance and Environmental Impact*, edited by J. W. Hurrell et al., AGU, Washington, D. C., doi:10.1029/134GM01.

Huybers, P., G. Gebbie, and O. Marchal (2007), Can paleoceanographic tracers constrain meridional circulation rates?, *J. Phys. Oceanogr.*, *37*(2), 394–407.

Iacono, M. J., J. S. Delamere, E. J. Mlawer, M. W. Shephard, S. A. Clough, and W. D. Collins (2008), Radiative forcing by long-lived greenhouse gases: Calculations with the AER radiative transfer models, *J. Geophys. Res.*, *113*, D13103, doi:10.1029/2008JD009944.

Jungclaus, J., N. Fischer, H. Haak, K. Lohmann, J. Marotzke, D. Matei, U. Mikolajewicz, D. Notz, and J. Storch (2013), Characteristics of the ocean simulations in the Max Planck Institute Ocean Model (MPIOM) the ocean component of the MPI-Earth system model, *J. Adv. Model. Earth Syst.*, *5*, 422–446, doi:10.1002/jame.20023.

Jungclaus, J. H., H. Haak, M. Latif, and U. Mikolajewicz (2005), Arctic-North Atlantic interactions and multidecadal variability of the meridional overturning circulation, *J. Clim.*, *18*(19), 4013–4031.

Keigwin, L. D., and E. A. Boyle (2008), Did north Atlantic overturning halt 17,000 years ago?, *Paleoceanography*, *23*, PA1101, doi:10.1029/2007PA001500.

Knight, J., R. Allan, C. Folland, M. Vellinga, and M. Mann (2005), A signature of persistent natural thermohaline circulation cycles in observed climate, *Geophys. Res. Lett.*, *32*, L20708, doi:10.1029/2005GL024233.

Koenigk, T., U. Mikolajewicz, J. H. Jungclaus, and A. Kroll (2009), Sea ice in the Barents Sea: Seasonal to interannual variability and climate feedbacks in a global coupled model, *Clim. Dyn.*, *32*(7–8), 1119–1138.

Kwon, Y.-O., and C. Frankignoul (2014), Mechanisms of multidecadal Atlantic meridional overturning circulation variability diagnosed in depth versus density space, *J. Clim.*, *27*(24), 9359–9376.

Lamy, F., H. W. Arz, G. C. Bond, A. Bahr, and J. Pätzold (2006), Multicentennial-scale hydrological changes in the black sea and northern red sea during the Holocene and the arctic/north Atlantic oscillation, *Paleoceanography*, *21*, PA1008, doi:10.1029/2005PA001184.

Latif, M., and N. S. Keenlyside (2011), A perspective on decadal climate variability and predictability, *Deep Sea Res., Part II*, *58*(17), 1880–1894.

Latif, M., et al. (2004), Reconstructing, monitoring, and predicting multidecadal-scale changes in the north Atlantic thermohaline circulation with sea surface temperature, *J. Clim.*, *17*(7), 1605–1614.

Latif, M., C. Böning, J. Willebrand, A. Biastoch, J. Dengg, N. Keenlyside, U. Schweckendiek, and G. Madec (2006), Is the thermohaline circulation changing?, *J. Clim.*, *19*(18), 4631–4637.

Leith, C. (1973), The standard error of time-average estimates of climatic means, *J. Appl. Meteorol.*, *12*(6), 1066–1069.

Leppäranta, M. (1983), A growth model for black ice, snow ice, and snow thickness in subarctic basins, *Nord. Hydrol.*, *14*, 59–70.

Li, L., P. Lin, Y. Yu, B. Wang, T. Zhou, L. Liu, J. Liu, Q. Bao, S. Xu, W. Huang, et al. (2013), The flexible global ocean-atmosphere-land system model, Grid-point Version 2: FGOALS-g2, *Adv. Atmos. Sci.*, *30*, 543–560.

Lohmann, G. (1998), The influence of a near-bottom transport parameterization on the sensitivity of the thermohaline circulation, *J. Phys. Oceanogr.*, *28*(10), 2095–2103.

Lohmann, G. (2016), Atmospheric bridge on orbital time scales: Theoretical and applied climatology, *Theor. Appl. Climatol.*, 1–10, doi: 10.1007/s00704-015-1725-2.

Lohmann, G., and R. Gerdes (1998), Sea ice effects on the sensitivity of the thermohaline circulation, *J. Clim.*, *11*(11), 2789–2803.

Lohmann, G., M. Pfeiffer, T. Laepple, G. Leduc, and J.-H. Kim (2013), A model-data comparison of the Holocene global sea surface temperature evolution, *Clim. Past*, (*9*), 1807–1839.

Lott, F. (1999), Alleviation of stationary biases in a GCM through a mountain drag parameterization scheme and a simple representation of mountain lift forces, *Mon. Weather Rev.*, *127*(5), 788–801.

Loveland, T., B. Reed, J. Brown, D. Ohlen, Z. Zhu, L. Yang, and J. Merchant (2000), Development of a global land cover characteristics database and IGBP DISCover from 1 km AVHRR data, *Int. J. Remote Sens.*, *21*(6–7), 1303–1330.

Mahajan, S., R. Zhang, and T. L. Delworth (2011), Impact of the Atlantic meridional overturning circulation (AMOC) on Arctic surface air temperature and sea ice variability, *J. Clim.*, *24*(24), 6573–6581.

Marsland, S. J., H. Haak, J. H. Jungclaus, M. Latif, and F. Röske (2003), The Max-Planck-Institute global ocean/sea ice model with orthogonal curvilinear coordinates, *Ocean Modell.*, *5*(2), 91–127, doi:10.1016/S1463-5003(02)00015-X.

McManus, J., R. Francois, J.-M. Gherardi, L. Keigwin, and S. Brown-Leger (2004), Collapse and rapid resumption of Atlantic meridional circulation linked to deglacial climate changes, *Nature*, *428*(6985), 834–837.

Müller, J., G. Massé, R. Stein, and S. T. Belt (2009), Variability of sea-ice conditions in the Fram Strait over the past 30,000 years, *Nat. Geosci.*, *2*(11), 772–776.

Otto-Bliesner, B. L., E. C. Brady, G. Clauzet, R. Tomas, S. Levis, and Z. Kothavala (2006), Last Glacial Maximum and Holocene climate in CCSM3, *J. Clim.*, *19*(11), 2526–2544.

Owens, W., and P. Lemke (1990), Sensitivity studies with a sea ice-mixed layer-pycnocline model in the Weddel Sea, *J. Geophys. Res.*, *95*(C6), 9527–9538.

Parker, D., C. Folland, A. Scaife, J. Knight, A. Colman, P. Baines, and B. Dong (2007), Decadal to multidecadal variability and the climate change background, *J. Geophys. Res.*, *112*, D18115, doi:10.1029/2007JD008411.

Parkinson, C., and W. Washington (1979), A large-scale numerical model of sea ice, *J. Geophys. Res.*, *84*(C1), 311–337.

Pickart, R. S., M. A. Spall, M. H. Ribergaard, G. Moore, and R. F. Milliff (2003), Deep convection in the irminger sea forced by the greenland tip jet, *Nature*, *424*(6945), 152–156.

Polyakov, I., U. Bhatt, H. Simmons, D. Walsh, J. Walsh, and X. Zhang (2005), Multidecadal variability of North Atlantic temperature and salinity during the twentieth century, *J. Clim.*, *18*(21), 4562–4581.

Proshutinsky, A., D. Dukhovskoy, M.-L. Timmermans, R. Krishfield, and J. L. Bamber (2015), Arctic circulation regimes, *Philos. Trans. R. Soc. A*, *373*(2052), 20140160.

Raddatz, T., C. Reick, W. Knorr, J. Kattge, E. Roeckner, R. Schnur, K.-G. Schnitzler, P. Wetzel, and J. Jungclaus (2007), Will the tropical land biosphere dominate the climate-carbon cycle feedback during the twenty-first century?, *Clim. Dyn.*, *29*(6), 565–574.

Rasmussen, T. L., and E. Thomsen (2010), Holocene temperature and salinity variability of the Atlantic water inflow to the Nordic seas, *Holocene*, *20*(8), 1223–1234.

Redi, M. (1982), Oceanic isopycnal mixing by coordinate rotation, *J. Phys. Oceanogr.*, *12*, 1154–1158.

Reick, C., T. Raddatz, V. Brovkin, and V. Gayler (2013), Representation of natural and anthropogenic land cover change in MPI-ESM, *J. Adv. Model. Earth Syst.*, *5*, 459–482, doi:10.1002/jame.20022.

Renssen, H., H. Goosse, T. Fichefet, V. Brovkin, E. Driesschaert, and F. Wolk (2005), Simulating the Holocene climate evolution at northern high latitudes using a coupled atmosphere-sea ice-ocean-vegetation model, *Clim. Dyn.*, *24*(1), 23–43.

Rimbu, N., G. Lohmann, J.-H. Kim, H. Arz, and R. Schneider (2003), Arctic/north Atlantic oscillation signature in Holocene sea surface temperature trends as obtained from alkenone data, *Geophys. Res. Lett.*, *30*(6), 1280, doi:10.1029/2002GL016570.

Roeckner, E., L. Dümenil, E. Kirk, F. Lunkeit, M. Ponater, B. Rockel, R. Sausen, and U. Schlese (1989), The Hamburg version of the ECMWF model (ECHAM), *Tech. Rep.*, *13*, World Meteorol. Org., Geneva, Switzerland.

Roeckner, E., R. Brokopf, M. Esch, M. Giorgetta, S. Hagemann, L. Kornblueh, E. Manzini, U. Schlese, and U. Schulzweida (2004), The atmospheric general circulation model echam5. Part II: Sensitivity of simulated climate to horizontal and vertical resolution, report no. 354, pp. 1–64, Hamburg, Gernamy.

Rühlemann, C., S. Mulitza, G. Lohmann, A. Paul, M. Prange, and G. Wefer (2004), Intermediate depth warming in the tropical Atlantic related to weakened thermohaline circulation: Combining paleoclimate and modeling data for the last deglaciation, *Paleoceanography*, *19*, PA1025, doi:10.1029/2003PA000948.

Schlesinger, M. E., and N. Ramankutty (1994), An oscillation in the global climate system of period 65–70 years, *Nature*, (*367*), 723–726.

Schmidt, G. A., et al. (2014), Configuration and assessment of the GISS ModelE2 contributions to the CMIP5 archive, *J. Adv. Model. Earth Syst.*, *6*, 141–184, doi:10.1002/2013MS000265.

Schneck, R., C. H. Reick, and T. Raddatz (2013), Land contribution to natural CO_2 variability on time scales of centuries, *J. Adv. Model. Earth Syst.*, *5*, 354–365, doi:10.1002/jame.20029.

Scholz, P., G. Lohmann, Q. Wang, and S. Danilov (2013), Evaluation of a Finite-Element Sea-Ice Ocean Model (FESOM) set-up to study the interannual to decadal variability in the deep-water formation rates, *Ocean Dyn.*, *63*(4), 347–370.

Scholz, P., D. Kieke, G. Lohmann, M. Ionita, and M. Rhein (2014), Evaluation of Labrador sea water formation in a global finite-element sea-ice ocean model setup, based on a comparison with observational data, *J. Geophys. Res.: Oceans*, *119*, 1644–1667, doi:10.1002/2013JC009232.

Semtner, A. (1976), A model for the thermodynamic growth of sea ice in numerical investigations of climate, *J. Phys. Oceanogr.*, *6*(3), 379–389.

Sidorenko, D., Q. Wang, S. Danilov, and J. Schröter (2011), FESOM under coordinated ocean-ice reference experiment forcing, *Ocean Dyn.*, *61*, 881–890, doi:10.1007/s10236-011-0406-7.

Sidorenko, D., et al. (2014), Towards multi-resolution global climate modeling with ECHAM6-FESOM. Part I: Model formulation and mean climate, *Clim. Dyn.*, *44*, 757–780, doi:10.1007/s00382-014-2290-6.

Steele, M., and T. Boyd (1998), Retreat of the cold halocline layer in the arctic ocean, *J. Geophys. Res.*, *103*(C5), 10,419–10,435.

Stevens, B., et al. (2013), Atmospheric component of the MPI-M Earth System Model: ECHAM6, *J. Adv. Model. Earth Syst.*, *5*, 146–172, doi:10.1002/jame.20015.

Stommel, H. (1961), Thermohaline convection with two stable regimes of flow, *Tellus*, *13*(2), 224–230.

Storch, J.-S. v., C. Eden, I. Fast, H. Haak, D. Hernández-Deckers, E. Maier-Reimer, J. Marotzke, and D. Stammer (2012), An estimate of the Lorenz energy cycle for the world ocean based on the STORM/NCEP simulation, *J. Phys. Oceanogr.*, *42*(12), 2185–2205.

Sun, C., J. Li, and F.-F. Jin (2015), A delayed oscillator model for the quasi-periodic multidecadal variability of the nao, *Clim. Dyn.*, *45*(7–8), 2083–2099.

Sundqvist, H., E. Berge, and J. E. Kristjánsson (1989), Condensation and cloud parameterization studies with a mesoscale numerical weather prediction model, *Mon. Weather Rev.*, *117*(8), 1641–1657.

Taylor, K. E., R. J. Stouffer, and G. A. Meehl (2012), An overview of CMIP5 and the experiment design, *Bull. Am. Meteorol. Soc.*, *93*(4), 485–498.

Thornalley, D. J., H. Elderfield, and I. N. McCave (2009), Holocene oscillations in temperature and salinity of the surface subpolar North Atlantic, *Nature*, *457*(7230), 711–714.

Timmermann, R., S. Danilov, J. Schröter, C. Böning, D. Sidorenko, and K. Rollenhagen (2009), Ocean circulation and sea ice distribution in a finite element global sea ice-ocean model, *Ocean Modell.*, *27*, 114–129.

Visbeck, M., H. Cullen, G. Krahmann, and N. Naik (1998), An ocean model's response to north Atlantic oscillation-like wind forcing, *Geophys. Res. Lett.*, *25*(24), 4521–4524.

Visbeck, M., E. P. Chassignet, R. G. Curry, T. L. Delworth, R. R. Dickson, and G. Krahmann (2003), The ocean's response to north Atlantic oscillation variability, in *The North Atlantic Oscillation: Climatic Significance and Environmental Impact*, edited by J. W. Hurrell, et al., pp. 113–145, AGU, Washington, D. C.

Voldoire, A., et al. (2013), The CNRM-CM5. 1 global climate model: Description and basic evaluation, *Clim. Dyn.*, *40*(9–10), 2091–2121.

Wang, Q., S. Danilov, D. Sidorenko, R. Timmermann, C. Wekerle, X. Wang, T. Jung, and J. Schröter (2013), The finite element sea ice-ocean model (FESOM): Formulation of an unstructured-mesh ocean general circulation model, *Geosci. Model Dev. Discuss.*, *6*, 3893–3976.

Watanabe, S., et al. (2011), MIROC-ESM 2010: Model description and basic results of CMIP5-20c3m experiments, *Geosci. Model Dev.*, *4*, 845–872.

Wei, W., and G. Lohmann (2012), Simulated Atlantic multidecadal oscillation during the Holocene, *J. Clim.*, *25*(20), 6989–7002.

Whitehead, J. (1998), Topographic control of oceanic flows in deep passages and straits, *Rev. Geophys.*, *36*(3), 423–440.

Wu, T., R. Yu, and F. Zhang (2008), A modified dynamic framework for the atmospheric spectral model and its application, *J. Atmos. Sci.*, *65*(7), 2235–2253.

Wu, T., R. Yu, F. Zhang, Z. Wang, M. Dong, L. Wang, X. Jin, D. Chen, and L. Li (2010), The Beijing Climate Center atmospheric general circulation model: Description and its performance for the present-day climate, *Clim. Dyn.*, *34*(1), 123–147.

Xu, X., M. Werner, M. Butzin, and G. Lohmann (2013), Oceanic d18o variation and its relation to salinity in the mpi-om ocean model, in *Earth System Science: Bridging the Gaps between Disciplines Perspectives From a Multi-disciplinary Helmholtz Research School*, edited by G. Lohmann, et al., pp. 70–74, Springer, Heidelberg, Germany.

Yeager, S., and G. Danabasoglu (2012), Sensitivity of Atlantic meridional overturning circulation variability to parameterized Nordic sea overflows in ccsm4, *J. Clim.*, *25*(6), 2077–2103.

Yukimoto, S., et al. (2012), A new global climate model of the Meteorological Research Institute: MRI-CGCM3-model description and basic performance, *J. Meteorol. Soc. Jpn.*, *90*, 23–64.

Zhang, R. (2007), Can the Atlantic Ocean drive the observed multidecadal variability in northern hemisphere mean temperature?, *Geophys. Res. Lett.*, *34*, L02709, doi:10.1029/2006GL028683.

Zhang, R. (2008), Coherent surface-subsurface fingerprint of the Atlantic meridional overturning circulation, *Geophys. Res. Lett.*, *35*, L20705, doi:10.1029/2008GL035463.

Zhang, R. (2015), Mechanisms for low-frequency variability of summer arctic sea ice extent, *Proc. Natl. Acad. Sci. U. S. A.*, *112*(15), 4570–4575.

Zheng, W., and Y. Yu (2013), Paleoclimate simulations of the mid-Holocene and Last Glacial Maximum by FGOALS, *Adv. Atmos. Sci.*, *30*, 684–698.